Winter 2017

Transparent Phased Patch Antenna Array for Beamsteering Applications

Cyle Ziegler
University of New Hampshire, Durham

Transparent Phased Patch Antenna Array for Beamsteering Applications

By

Cyle W. Ziegler

Bachelor of Science in Electrical Engineering, University of New Hampshire, 2016

Thesis

Submitted to the University of New Hampshire

in Partial Fulfillment of

the Requirements for the Degree of

Master of Science

in

Electrical Engineering

December, 2017

This thesis has been examined and approved in partial fulfillment of the requirements for the degree of Master of Science in Electrical Engineering by:

Thesis Director, Nicholas J. Kirsch, Ph.D.
Associate Professor (Electrical and Computer Engineering)

Kent A. Chamberlin, Ph.D.
Professor and Chair (Electrical and Computer Engineering)

Michael J. Carter, Ph.D., P.E.
Associate Professor (Electrical and Computer Engineering)

Wayne J. Smith, Ph.D.
Senior Lecturer (Electrical and Computer Engineering)

on 12/6/2017.

Original approval signatures are on file with the University of New Hampshire Graduate School.

DEDICATION

I would like to dedicate this thesis to my better half, Tristan Ramey, my dad, Gary Ziegler, my mom, Cathy Foley, and my siblings, Jess Hebert, Nick Hebert, and Kaitlin Scanlon.

ACKNOWLEDGEMENT

I would like to thank Dr. Nicholas Kirsch for advising me on the work associated with this thesis project. This opportunity provided me with the ability to continue my education at the University of New Hampshire. A special thanks to Mr. Brough Turner and Dr. George Kontopidis of netBlazr who are responsible for the creation of this project.

I would like to thank the other members of my committee, Dr. Kent Chamberlin, Dr. Michael Carter, and Dr. Wayne Smith. Their enthusiasm for the course material was paramount for the enjoyment felt throughout this program, and they have shown me what it means to be an educator. I would also like to thank them for their impact and assistance on this thesis project.

I would also like to thank my fellow graduate students Jean Lambert Kubwimana, Mahdi Al Badrawi, and Jon Tefft from the Wireless Systems Laboratory. They assisted with experimental setups and discussions of results obtained. I'd like to thank Ben Mitchell and Scott Campbell who assisted with machining parts in the machine shop. I'd like to thank Tristan Ramey, Peter Abdu, and Ron Totten who assisted with formatting and editing. Lastly, thank you to my family and friends who supported me throughout my education.

Contents

List of Tables

List of Figures

ABSTRACT

Transparent Phased Patch Antenna Array for Beamsteering Applications

by

Cyle W. Ziegler

University of New Hampshire, December 2017

The ever expanding demand for wireless communications faces many challenges. As the necessity for wireless communications increases, inevitably, the impact wireless communications systems have on their environment will also increase. This is important because the environmental impact a communications system has may limit the locations in which that system can be deployed. For this reason, there is a demand for unobtrusive hardware in order to grow the wireless communications infrastructure. Furthermore, performance limiting factors associated with wireless communications can be mitigated by implementing steerable antennas, making a less obtrusive steerable antenna desired. The contribution of this work is the demonstration of a vertically-polarized transparent patch antenna array and a horizontally-polarized transparent patch antenna array for beamsteering applications. Details regarding element array spacing, materials used, parameters, simulated and measured performance values, and analysis of each array will be covered in this thesis.

CHAPTER 1

Introduction

From the 1880's through the 1890's the world began to change in ways that seemed unimaginable. This age was known as the birth of the radio. Heinrich Rudolph Hertz, a German physicist, dedicated his work to proving the existence of electromagnetic radiation, a theory developed by James Clerk Maxwell. Hertz was successful in his efforts, demonstrating what was then called wireless telegraphy; transferring energy between two unattached devices [3]. This scientific development sparked innovation within Italian inventor Guglielmo Marconi. By 1901, Marconi had designed a wireless telegraphy system based on the use of Hertzian waves, or radio waves, to successfully transmit energy across the Atlantic Ocean [4]. From this development, communication worldwide was changed.

Great technological advancements have been made in the last hundred plus years since the first wireless telegraphic breakthrough. Today, nearly everyone relies on wireless communications for safety, business, and personal use. However, the increasing demand for wireless communications requires more infrastructure. This chapter will present limiting factors of wireless communications hardware, the benefits of implementing transparent steerable antennas, specifications pertaining to the systems in this thesis project, this project's contribution to science, and the organization of this thesis.

1.1 Limiting Factors of Communications Hardware

The wireless user space has continued to explode in size and currently supports more than seven billion mobile devices. Although the convenience and flexibility of wireless communication is driving its ever expanding infrastructure, wireless faces many challenges. Importantly, the distance through which a signal can be transmitted is limited by propagation losses [5]. In order to transmit a signal at greater distances, the transmit power must be increased. Unfortunately, increasing the transmit power of a system may cause interference to adjacent systems operating in the same frequency band. This is a common problem with wireless communication systems.

Figure 1.1: An antenna disguised as a tree to reduce its obtrusiveness to the environment [1].

Environmental constraints are a factor in the locations that wireless communications systems are deployed. This is because interactions between transmitted radiation and materials that exist within that environment may limit connectivity distances. In order to maximize performance, antennas are placed in unobstructed and elevated positions. Traditionally, antenna towers are utilized as an elevated location to mount wireless communications systems. These towers are visually obtrusive to their surrounding environment, and in some cases, erecting a tower within a desired location is not feasible. Rooftops and balconies of tall buildings have also been used as mounting locations. However, these locations are constrained

by cost, safety, and permission from building owners. For these reasons, attempts have been made to disguise antennas within their surrounding environment, which reduces their visual impact. Figure 1.1 is an example of an antenna that is disguised as a tree in order to reduce obtrusiveness in its surrounding environment.

1.2 Benefits of Steerable Transparent Antennas

Directional antennas steer energy to mitigate propagation losses and interference [5]. Focusing energy in a specific directions applies more energy to that direction, resulting in a longer propagation distance. Furthermore, directionally controlling transmissions greatly reduces interference because the wireless communications system only produces incident energy in a desired direction.

Transparent directional antennas are less obtrusive than opaque directional antennas. Transparent antennas have a wider range of deployment options than opaque antennas, such as the ability to be mounted in the window of a tall building. Figure 1.2 shows how an opaque and a transparent antenna would look within a window mounted environment. The opaque antennas would obstruct the view from the window and would block valuable sunlight from passing through the window. The transparent antenna, however, minimally obstructs the view from the window and would allow nearly all valuable sunlight to pass through the window. For this reason, transparent antennas are a more suitable antenna to be deployed in a window.

Figure 1.2: Comparing the obtrusiveness of an opaque antenna to a transparent antenna mounted in a window [2].

1.3 System Specifications

The aim of this research is to develop a transparent directional antenna in order to facilitate the spread of high speed internet connectivity. The antennas developed for this thesis operate in the 5-6 GHz frequency band in order to support the expansion of the wireless communications infrastructure. This frequency band is important because wireless applications using the unlicensed spectrum in the 5-6 GHz frequency band are gaining popularity [6]. Transparent conductive materials will be utilized in order to construct the transparent antenna system. Previous experiments, comparing transparent conductive material performance when implemented in antennas, revealed that conductive mesh materials have high performance compared to other transparent conductive materials [6] [7]. As such, thin conductive mesh technology was used to fabricate the transparent antennas.

The array feed network in this thesis project has the capability to support four steering angles. These four antenna functions were facilitated by implementing a two bit control circuit and a Butler matrix. Explanations and analysis of these functions are covered in Chapter 3 of this thesis.

1.4 Contribution

The contribution of this work is the demonstration of a vertically-polarized transparent antenna and a horizontally-polarized transparent antenna. The transparent antennas are deployed as a phased array of patch antennas supporting beamsteering applications. The phased array system has the functionality of a directive antenna with the benefits of control, which mitigates performance limiting factors associated with wireless communications. Furthermore, the optically transparent elements within the system greatly reduce the antennas obtrusiveness, providing unobtrusive antenna options for specific deployable environments.

1.5 Thesis Organization

This section provides an explanation of each chapter of this thesis. This section helps the reader navigate this thesis and facilitates efficiency when particular sections are needed for review or reference.

Chapter 2 presents background information pertaining to this thesis project. Fundamental concepts required for understanding the design and experimental results of this thesis project are explained.

Chapter 3 presents the design of the transparent and opaque antennas. This chapter utilizes the information provided in Chapter 2 in order to derive the parameters of the transparent and opaque antennas. The design chapter is important because it provides an understanding of system performances prior to fabrication. Simulations save valuable time, money, and effort. Furthermore, the simulations conducted in the design step of this project provide valuable data. The simulation data is used to validate the measured data of the fabricated systems.

Chapter 4 presents the procedure used to fabricate the transparent and opaque antennas. This chapter is important because it provides specific information on how this project can be replicated. This chapter can also be referenced in order to facilitate other research projects that involve similar materials or processes.

Chapter 5 presents empirical results, comparing simulated values to measured values. Tables and figures are provided in this chapter in order to organize results. The analytic information presented in this chapter proves this thesis is a contribution to science.

Chapter 6 concludes this thesis project, summarizing the results and the impact of the project.

Chapter 7 presents a focus for future work on this project. This chapter is important because it provides insight on what research needs to be conducted in order to increase the contribution of the systems presented in this thesis project.

CHAPTER 2

Background Information

Parameters, properties, and materials are defined and conceptualized in this chapter. This information is presented in support of the experimental process and results of this thesis project. The fundamentals of electromagnetism are essential to this research, making this chapter very important. The first portion of this chapter explains basic electromagnetic constitutive parameters. Secondly, two-port networks are explained so that basic system functions and the relationships between transmitted energy and received energy is understood. Then, index of refraction is explained. Index of refraction is included to show how transmitted energy interacts with boundary layers of different material. Fourthly, the skin effect is explained. The skin effect explains how energy travels through a material. Next, transparent conductive material parameters is presented, providing information on multiple transparent conductive materials. The transparent conductive material section also explains parameters of the conductive mesh technology used in this thesis project. The remaining topics covered in this chapter are basic antenna parameters, microstrip transmission lines, microstrip patch antennas, and antenna arrays. These sections explain concepts required to understand antenna performance. Furthermore, these antenna sections mathematically explain how to design specific antenna parameters. These processes are important because Chapter 3 uses these processes to design the transparent and opaque antennas. Lastly, this chapter presents the software and hardware used in the execution of this thesis project.

2.1 Constitutive Parameters

This section defines what the constitutive parameters are and their relevance in electromagnetism. A constitutive relation in electromagnetism is specific to the dynamics of free charges to current, or the dynamics of bound charges to current. The parameters that are used to balance these relationships are permittivity, permeability, and conductivity. It is important to know that these parameters may vary within a material due to varying material properties. Four material properties that significantly affect constitutive parameters are homogeneity, linearity, dispersion, and isotropy. A material is homogeneous when the constitutive parameters do not vary with position within that material. Secondly, a material is linear if the constitutive parameters do not vary within that material due to a change in applied field intensity. Thirdly, a material is non-dispersive if the constitutive parameters do not vary with frequency in that material. Lastly, a material is isotropic if the constitutive parameters do not vary with direction in that material [8]. The properties of a material are important in accurately calculating the constitutive parameters.

2.1.1 Dielectric Permittivity

Dielectric permittivity (ϵ), in units of farads per meter ($\frac{F}{m}$), is the measure of how an electric field affects, and is affected by, an electrical insulator or dielectric material placed in the field [9]. This measurement of a dielectric material is known as the dielectric constant and is defined by the relative permittivity (ϵ_r) and the permittivity in free space (ϵ_0). Relative permittivity is a proportional constant used to describe a material's dielectric constant relative to that of free space, shown in (2.1) [10]. Permittivity relates the electric field (E) to electric flux density (D), shown in (2.2).

$$\epsilon = \epsilon_r \epsilon_0 \tag{2.1}$$

$$D = \epsilon E \tag{2.2}$$

Dielectric permittivity may vary with the frequency of an applied electric field, humidity, temperature, and other parameters [11]. Frequency dependence will cause distortion in broad-band antenna applications. Furthermore, the polarization of the dielectric material is not instantaneous to an applied field. This delay results in a causal response which can be represented by a phase shift, requiring that ϵ is treated as a complex function of angular frequency, ω, of the applied electric field. Since complex numbers specify both magnitude and phase, the relationship between D and E becomes (2.3) [12].

$$D_0 e^{-i\omega t} = \hat{\epsilon}(\omega) E_0 e^{-i\omega t} \tag{2.3}$$

2.1.2 Permeability

Permeability (μ), in units of Henrys per meter ($\frac{H}{m}$), measures the ability of a material to affect a magnetic field in response to an applied magnetic field. This measurement consists of relative permeability (μ_r) and the permeability in free space (μ_0). Relative permeability is a proportional constant used to describe a material's permeability relative to that of free space, shown in (2.4). Permeability relates the magnetic field (H) to magnetic flux density (B), shown in (2.5) [13]. The relative permeability for all calculations within this thesis project is unity.

$$\mu = \mu_r \mu_0 \tag{2.4}$$

$$B = \mu H \tag{2.5}$$

2.1.3 Conductivity

A material is an electrical conductor if it has free electrons that can drift in an electric field [14]. Conductivity (σ), with units of Siemens per meter ($\frac{S}{m}$), is a measure of how easily an electric current can flow through a material [15]. Conductivity relates an applied electric field (E) to a material's surface current density (J). This relationship is shown in (2.6).

$$J = \sigma E \tag{2.6}$$

2.2 Two-Port Networks

This section defines the parameters used to measure and analyze a two-port network. A port is defined as having two terminals where a current applied to one of the terminals must equal the current exiting the other terminal. This is known as the port condition [16]. In two-port networks, shown in fig. 2.1, there are two pairs of terminals to connect external circuitry. This model of a two-port network is commonly used to analyze large circuits by isolating portions of the circuit. Instead of solving for all internal voltages and currents, signals are applied to the ports and the network response to those signals is analyzed [17]. Scattering (S), impedance (Z), and relative representation of impedance (ABCD) are parameters that define the function of a two-port network, and are used in this thesis project.

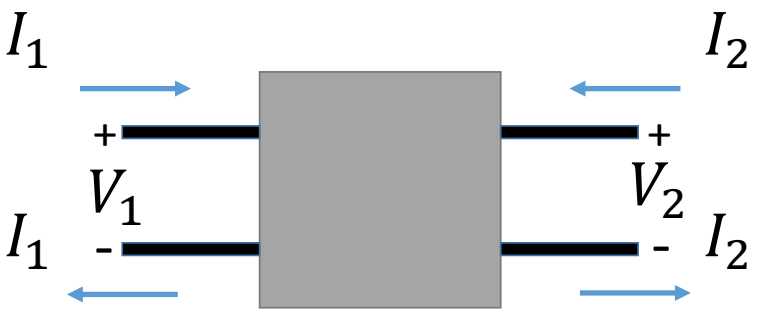

Figure 2.1: Block diagram of a two-port network with associated voltages and current.

2.2.1 Scattering Parameters

S-parameters, widely used in radio frequency (RF) network analysis, use matched input and output load impedances to calculate power transfer within a network. The efficiency of a network is calculated from the incident and reflected power of the network. (2.7) shows the relationship between the incident normalized power wave (a_n) and the reflected normalized power wave (b_n).

$$\begin{bmatrix} b_1 \\ b_2 \end{bmatrix} = \begin{bmatrix} S_{11} & S_{12} \\ S_{21} & S_{22} \end{bmatrix} * \begin{bmatrix} a_1 \\ a_2 \end{bmatrix} \tag{2.7}$$

The S_{xy}-matrix, y describing the port in which the incident power wave is applied and x describing the port in which the transmitted power wave egresses, is a matrix of complex numbers because the RF energy experiences attenuation and phase change throughout the network [18]. Within the S_{xy}-matrix, S_{11} is known as the reflection coefficient and S_{21} is known as the transmission coefficient. The reflection coefficient, an amplitude ratio comparing the reflected wave to the incident wave, is the amount of RF energy reflected within a network due to impedance discontinuities, as measured by the amount of RF energy returned to the generator [19]. The transmission coefficient is an amplitude ratio comparing the complex transmitted wave to the incident wave after it experiences discontinuities within the network. The transmission coefficient is used to measure how much RF energy is transmitted through the network [20].

2.2.2 Impedance Parameters

Z-parameters relate port voltages and currents. For a two-port network, the open circuit method is utilized. A current is applied to one port and the remaining port is terminated by its characteristic impedance, so that both port voltages can be measured and the Z_{xy}-matrix can be solved. (2.8) shows this relationship [21].

$$\begin{bmatrix} V_1 \\ V_2 \end{bmatrix} = \begin{bmatrix} Z_{11} & Z_{12} \\ Z_{21} & Z_{22} \end{bmatrix} * \begin{bmatrix} I_1 \\ I_2 \end{bmatrix} \tag{2.8}$$

The Z_{xy}-matrix, y describing which port voltage is referred to and x describing which port current is referred to, is a matrix of complex numbers that describe the amount of resistance and reactance that exist within the network. Using values from the Z_{xy}-matrix, the input (2.9) and output impedance (2.10) of a network can be calculated, where Z_S is the source impedance connected to port 1 and Z_L is the external load impedance connected to port 2 [22].

$$Z_{in} = Z_{11} - \frac{Z_{12} * Z_{21}}{Z_{22} * Z_L} \tag{2.9}$$

$$Z_{out} = Z_{22} - \frac{Z_{12} * Z_{21}}{Z_{11} * Z_S} \tag{2.10}$$

2.2.3 ABCD Parameters

$ABCD$-parameters, commonly known as transmission line parameters, have certain characteristics depending on what type of network is being analyzed. In this experiment, a reciprocal network is analyzed. A reciprocal network consists entirely of linear passive components such as resistors, capacitors, and inductors. For a reciprocal network, (2.11) is true [23]. Furthermore, $ABCD$-parameters are derived similarly to Z-parameters. The difference in derivation methods is the way port voltages and currents are compared. This difference is shown in (2.12).

$$AD - BC = 1 \tag{2.11}$$

$$\begin{bmatrix} V_1 \\ I_1 \end{bmatrix} = \begin{bmatrix} A & B \\ C & D \end{bmatrix} * \begin{bmatrix} V_2 \\ -I_2 \end{bmatrix} \tag{2.12}$$

Relating Z-parameters directly to $ABCD$-parameters is very useful in certain applications, and this relationship is used in Appendix C. A network analyzer allows the Z-parameters of a network to be measured in experimental analysis. $ABCD$-parameters can then be derived from the measured Z-parameters (2.13) [24].

$$A = \frac{Z_{11}}{Z_{21}}, B = \frac{Z_{11} * Z_{22} - Z_{21}^2}{Z_{21}}, C = \frac{1}{Z_{21}}, D = \frac{Z_{22}}{Z_{21}} \tag{2.13}$$

2.3 Index of Refraction

The index of refraction, n, is a dimensionless parameter that represents the amount of bending a wave encounters when it passes from one medium into another. It is equal to $\sqrt{\epsilon_r}$ [25]. This parameter is used in Snell's law. Snell's law compares the angle of incidence and angle of transmittance, θ_1 and θ_2 respectively, on a boundary between two different media using the material's intrinsic impedance, η. Snell's law is given in (2.14) and is visually depicted in fig. 2.2.

$$\eta_1 \sin\theta_1 = \eta_2 \sin\theta_2 \tag{2.14}$$

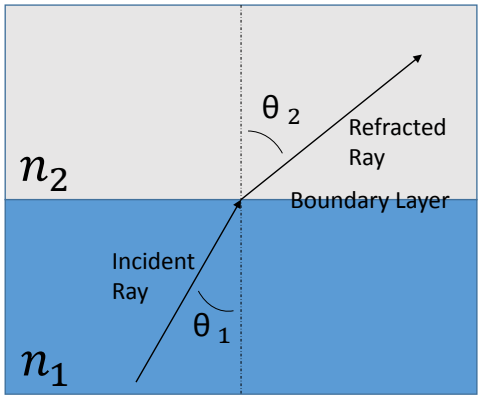

Figure 2.2: An incident wave passes through a boundary at angle θ_1 relative to normal to the boundary and refracts at angle θ_2.

The relative permeability of a dielectric material is unity. Using this, the relationship between intrinsic impedance and the index of refraction is derived in (2.15)-(2.22). The index of refraction for a wave propagating through a boundary is vital because it determines the direction of the transmitted wave after it passed through a boundary [26].

$$\eta_1 \sin\theta_1 = \eta_2 \sin\theta_2 \tag{2.15}$$

$$\eta_1 = \omega\sqrt{\mu_0\epsilon_{r1}} \tag{2.16}$$

$$\omega\sqrt{\mu_0\epsilon_{r1}} \sin\theta_1 = \omega\sqrt{\mu_0\epsilon_{r2}} \sin\theta_2 \tag{2.17}$$

$$\frac{\omega\sqrt{\mu_0\epsilon_{r1}}}{\omega\sqrt{\mu_0\epsilon_{r2}}} \sin\theta_1 = \sin\theta_2 \tag{2.18}$$

$$\frac{\sqrt{\epsilon_{r1}}}{\sqrt{\epsilon_{r2}}} \sin\theta_1 = \sin\theta_2 \tag{2.19}$$

$$\sqrt{\epsilon_r} \sin\theta_1 = \sin\theta_2 \tag{2.20}$$

$$n = \sqrt{\epsilon_r} \tag{2.21}$$

$$n = \frac{\sin\theta_2}{\sin\theta_1} \tag{2.22}$$

2.4 Eddy Currents and Skin Effect

Eddy currents are loops of electrical current within a conductor that are the result of a changing magnetic field within the conductor. As the intensity of the magnetic field changes, so does the strength of eddy currents. Eddy currents flow perpendicular to the magnetic field and cause the effective resistance of the conductor to change as signal frequency changes [27]. Eddy currents diversify the current density within the conductor by opposing current flow in the center of the conductor and reinforcing it on the skin of the conductor.

A skin depth is defined as the area near a conductor's surface that holds the majority of the electric current that flows through that conductor. (2.23) shows the formula for calculating the skin depth (δ_s) of a given conductor with a known applied signal frequency. As shown, the skin depth is inversely proportional to the signal frequency (f), the conductivity (σ), and the permeability (μ) of the conductor; good conductors have a relative permeability of unity [28]. Furthermore, DC signals are not represented in this equation. DC signals create a constant magnetic field within the conductor which does not create eddy currents, leaving a uniform current distribution throughout the conductor with no skin effect.

$$\delta_s = \sqrt{\frac{1}{\sigma \mu \pi f}} \tag{2.23}$$

2.5 Transparent Conductive Materials

Transparent conductive materials can be used for a vast array of applications such as liquid crystal displays (LCD), touchscreens, Organic Light-Emitting Diodes (OLED), and Photovoltaics (PV) [29]. In antenna applications, the conductivity of the material used is important to the performance of the device. Three common types of transparent conductive materials are transparent conductive oxides (TCO), transparent conductive polymers (TCP), and thin wire meshes. The ideal transparent conductive material for this thesis project has optical properties similar to glass and an electrical conductivity similar to that of copper. To determine which material is most applicable for antenna applications, each material must first be understood. The following sections explain each of the three materials and their critical properties. Lastly, the transparent conductive material used for this thesis project is selected.

2.5.1 Transparent Conductive Oxides

Transparent conductive oxides (TCO) are thin films of optically transparent and electrically conductive material. TCOs have been widely used in opto-electronic devices including

liquid crystal displays, solar cells, and plasma displays [30] [31]. The greatest advantage of a TCO is its high optical transparency, as it can be up to 90% transparent [7]. While there is the possibility of being up to 90% transparent, the actual optical transparency of a transparent conductive film largely depends on the thickness of the film deposition and the intrinsic material properties [32]. The material properties of TCO result in high sheet resistance, which causes inefficiencies [33]. The highest electron mobility available with the current technology provides a sheet resistance of 4.6 $\frac{\Omega}{square}$ [7] [34]. The most common TCO, indium tin oxide (ITO), has a low resistivity and is roughly 80% transparent. One downside to this material, however, is that it is rare throughout the world and thus very expensive [29]. Additionally, studies have shown that the sheet resistance of TCOs can increase significantly with humidity. Deployed in an environment with a relative humidity of 85%, the sheet resistance of TCOs can increase by more than 150% within 10 hours [35].

2.5.2 Transparent Conductive Polymers

Transparent conductive polymers (TCP) are polymers that have conjugated double bonds that allow for conduction. These polymers are commonly derived from polyacetylene, polyaniline, polypyrrole, or polythiophenes [36]. Similar to TCOs, the conductivity of a TCP is inversely proportional to its transparency. The thicker the TCP film is on a surface, the lower the transparency is and the greater is the conductivity. Although the conductivity of TCP is much lower than that of TCO, the fact that TCP can be made into flexible films makes them desirable despite their lower conductivity [37]. The most popular TCP, Polystyrene Sulfonate (PEDOT-PSS), can be integrated within moving structures and is capable of conforming to non-flat surfaces [38]. TCPs can achieve 70 to 80% optical transparency, but they suffer from low conductivity (roughly $300 S/m$), and high sheet resistance (100 $\frac{\Omega}{square}$) [39].

2.5.3 Thin Wire Mesh

A thin wire mesh consists of two important components: the conductive wire and the transparent film. The conductive wire can be made out of various conductive metals such as copper, silver, or gold. The conductive wires are so thin and brittle that the wires alone would break very easily so a transparent film is used to maintain the geometry of the wire mesh and protect the mesh from its environment. Without the transparent film the wire mesh would easily break in multiple places, which would create discontinuity within the mesh making the material highly inefficient. The thin wire mesh has very high conductivity and variable transparency. The material can be made more or less transparent by changing the geometry of the mesh. This flexibility allows the material to be used over a range of different applications.

2.5.4 Thin Wire Mesh Parameters

The transparent conductive material selected for this thesis project is a thin wire mesh. The specific material geometry is shown in fig. 2.3, with the mesh line width, q, pitch, p, number of horizontal mesh lines, n, and number of vertical mesh lines, m. The optical transparency of the mesh material is calculated by comparing the percentage of non-mesh wire area to the total area of the material, seen in (2.24) [40]. According to Song *et al.*, optimal performance is achieved with a continuous conductive strip along the edges of a patch antenna because current density is highest at the edges of a material. Therefore only discrete dimensions allowing the element to have a conductive strip along the edges should be used for good antenna performance [33]. Thin wire mesh material with a pitch of 297 um and mesh width of 25.9 um has a transparency of 74.8% and a sheet resistance of 0.28 $\frac{\Omega}{square}$. Furthermore, this material is stable and is relatively flexible.

$$Transparency = \frac{(m-1)(n-1)p^2}{(n(q+p)-p)(m(q+p)-p)}\% \tag{2.24}$$

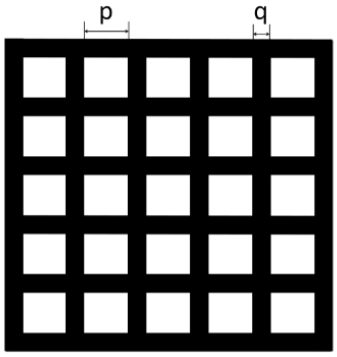

Figure 2.3: The physical structure and geometry of the thin wire mesh material with a solid conductive strip perimeter.

Table 2.1: Comparing Material Parameters

Material	Sheet Resistance ($\Omega/square$)	Optical Transparency (%)
TCP	100	80
TCO	4.6	90
Thin Wire Mesh	0.28	74.8

Table 2.1 compares the sheet resistance and transparency of the three different types of material [7] [41] [39]. While it is ideal to have a material with low sheet resistance and high optical transparency, the table shows that no single material is better in both categories. Low sheet resistance is most important for the performance of a conducting element and for this reason the thin wire mesh material was the best material to implement within a transparent antenna.

2.6 Fundamental Parameters of Antennas

This section defines parameters used to describe antenna performance, such as gain, bandwidth, radiation pattern, and beamwidth. With an understanding of these parameters, an antenna can be correctly analyzed for its function and capabilities. Mutual coupling, resonance, and quality factor are also discussed.

2.6.1 Gain

Gain is a measurement of the efficiency of the antenna and its directional capabilities, the relative intensity of the electromagnetic radiation at a certain angle from the antenna. When the gain of an antenna is reported without an angle, it is understood to be taken from the direction of maximum radiation [42]. This parameter is important because it defines the directional capability of an antenna.

2.6.2 Bandwidth

The signal bandwidth, in Hertz (Hz), refers to the frequency range within which the signal spectral density is within a defined range [43]. In this experiment, bandwidth for an antenna is defined as the range within which the reflection coefficient values are below -10 dB. This band describes the frequencies in which an antenna presents a nearly uniform impedance to a driving source.

2.6.3 Radiation Pattern

A radiation pattern refers to the angular dependence of the strength of the radio waves from an antenna or other signal source [44]. For the application addressed in this thesis project, only the far-field pattern is of interest. The far-field is a representation of distance from an antenna or source where electromagnetic radiation dominates the field without non-radiative near-field influence. Far-field is defined as the region in which the field acts as normal electromagnetic radiation. The far-field attenuates with distance from the source at a much slower rate than near-field [45]. The far-field radiation pattern is important in the analysis of an antenna because it shows the directional gain of the antenna.

2.6.4 Beamwidth

The beamwidth of an antenna is defined as the angular separation between two identical points on opposite sides of the radiation pattern maximum [42]. This experiment uses the

intersection of the sides of the pattern maximum and the -3 dB line from the maximum gain as the two identical points. This parameter is used to specify how an antenna's energy is focused.

2.6.5 Mutual Coupling

Mutual coupling is the electromagnetic interaction between antenna elements within an array. The current developed in each antenna element depends on its own excitation and contributions from adjacent antenna elements [46]. This mutual coupling between elements changes the performance of the overall antenna and can change the radiation pattern. The intensity of this performance change is inversely proportional to the distance between antenna elements, because the field strength of each component within the antenna system is strongest at its surface and reduces in intensity with distance from the surface [47]. As a result, one way to reduce mutual coupling between elements of a system is to increase element spacing.

2.6.6 Resonance and Quality Factor

Resonance occurs when a circuit has energy stored in both an electric field within a capacitor and a magnetic field flowing through an inductor. This energy is capable of transferring from one form to the other and can oscillate back and forth. The resonant frequency (f_0) of an element can be calculated using (2.25). The measure of how damped or under-damped an oscillation is defines the quality factor (Q-factor) [48]. The Q-factor of an element can be calculated using (2.26). If the Q-factor is high, the oscillation will release energy at a slow rate, causing the system energy to oscillate longer. If the Q-factor is low, the oscillation will release energy at a high rate, forcing the oscillation to diminish in a shorter period of time. The Q-factor also gives information on the bandwidth of an antenna. The 3 dB bandwidth of an antenna is calculated as the resonant frequency of the antenna divided by the Q-factor [49].

$$f_0 = \frac{1}{2\pi}\sqrt{\frac{1}{LC} - (\frac{R}{L})^2} \tag{2.25}$$

$$Q = \frac{1}{R}\sqrt{\frac{L}{C}} \tag{2.26}$$

2.7 Microstrip Transmission Lines

A microstrip transmission line is a type of electrical transmission line used to transmit RF signals. Figure 2.4 identifies the key components and physical parameters for a microstrip transmission line. One of the most important characteristics of a transmission line is its characteristic impedance. In order to calculate the impedance of a transmission line, the effective dielectric constant must be first calculated. The total derivation is shown in (2.27) through (2.32), where (W) is the width of the transmission line and (h) is the thickness of the dielectric material between the transmission line and the ground plane. Note that if (2.27) is true, (2.28) and (2.29) are used, but if (2.30) is true, then (2.31) and (2.32) are used.

$$\frac{W}{h} < 1 \tag{2.27}$$

$$\epsilon_{eff} = \frac{\epsilon_r + 1}{2} + \frac{\epsilon_r - 1}{2}[\frac{1}{\sqrt{1 + 12\frac{h}{W}}} + 0.04(1 - (\frac{W}{h}))^2] \tag{2.28}$$

$$Z_0 = \frac{60}{\sqrt{\epsilon_{eff}}} ln(8(\frac{h}{W}) + 0.25(\frac{W}{h})) \tag{2.29}$$

$$\frac{W}{h} > 1 \tag{2.30}$$

$$\epsilon_{eff} = \frac{\epsilon_r + 1}{2} + [\frac{\epsilon_r - 1}{2 * \sqrt{1 + 12(\frac{h}{W})}}] \tag{2.31}$$

$$Z_0 = \frac{120\pi}{\sqrt{\epsilon_{eff}}[\frac{W}{h} + 1.393 + \frac{2}{3} ln(\frac{W}{h} + 1.44)]} \tag{2.32}$$

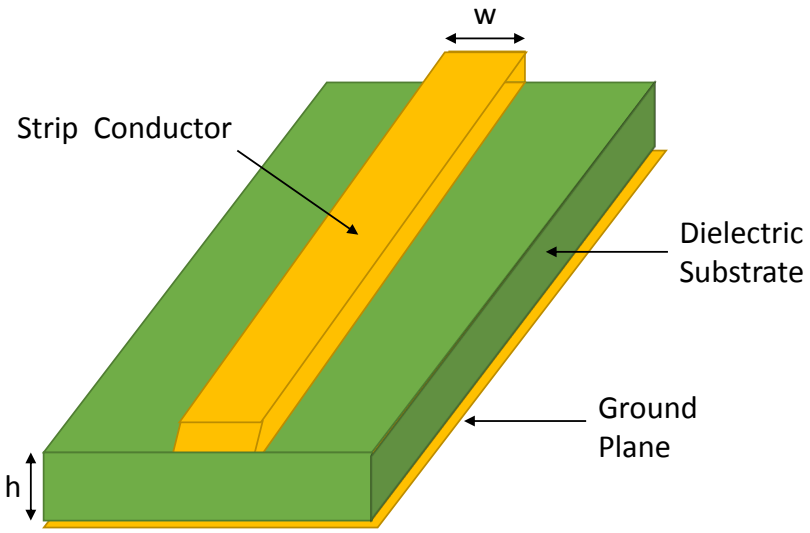

Figure 2.4: Isometric view of a microstrip transmission line.

2.7.1 Quarter-Wavelength Impedance Transformer

A microstrip transmission line with a quarter-wavelength impedance transformer was used in this thesis project. The impedance transformer was used to properly match the impedances within the network. It is important to match impedance within the network because it allows for maximum power transmission. Impedance mismatches in the network will reflect energy back into the system. Although an inset feed, explained later, was used to reduce the input impedance of the patch, the input impedance of the patch and the port impedance were not able to be matched without using an impedance transformer. Figure 2.5 shows a rectangular patch antenna with an edge fed transmission line. As is shown, there are three notable impedance values, Z_{in}, Z_0, and Z_L. Z_{in} is the transmission line that is matched to the incoming port, Z_0 is the quarter-wavelength impedance transformer, and Z_L is the impedance of the patch antenna. Using (2.33) the driving point impedance of the transmission line used as the quarter-wavelength impedance transformer is calculated.

$$Z_0 = \sqrt{Z_{in} Z_L} \tag{2.33}$$

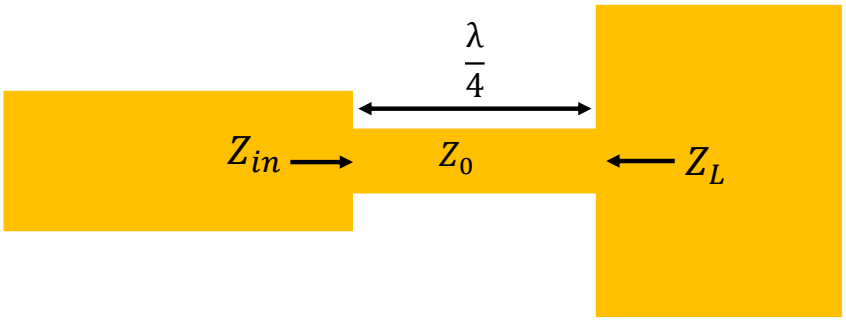

Figure 2.5: Diagram of the impedance transformer.

2.8 Microstrip Patch Antenna

A microstrip patch antenna is a directional antenna that can be easily fabricated using the printed circuit board process. For this thesis project, the individual antenna elements are microstrip patch antennas. In order to understand how these antennas were designed, one must first understand how they operate. This section provides important information on specific parameters and how a microstrip antenna operates.

Figure 2.6a shows the top view of a basic microstrip patch antenna. This figure includes two physical components: the microstrip transmission line and the microstrip antenna. The transmission line is explained in the next section. The patch antenna has three key physical parameters: height (h), width (W), and length (L). These physical parameters determine the antenna's resonant frequency, bandwidth, and input impedance. These parameters are explained mathematically for clarity.

The height of the dielectric material is the distance between the patch antenna and the ground plane, shown in fig. 2.6b. The height is typically much shorter than the operating wavelength, but not much shorter than $\frac{\lambda}{40}$ because heights less than that will cause the antenna to be less efficient.

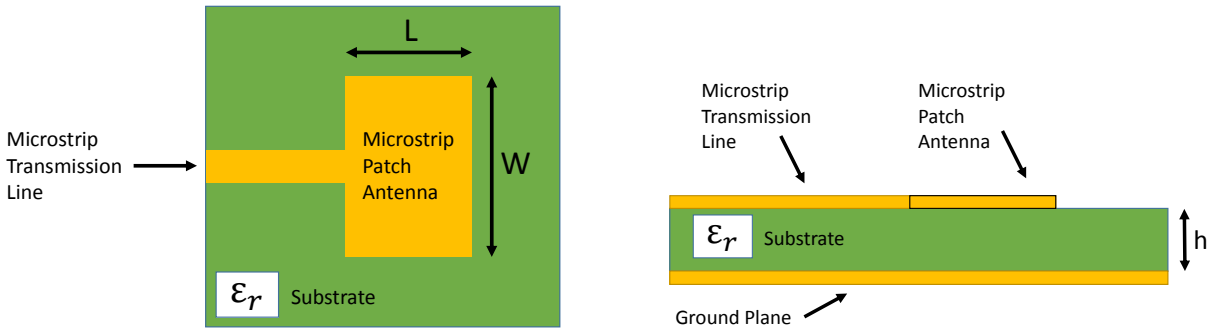

(a) Top view. (b) Side view.

Figure 2.6: Patch antenna physical parameters.

The width of a microstrip patch antenna, shown in fig. 2.6a, effects the input impedance. Increasing the width will lower the input impedance on the transmission line because the area in which free electrons flow increases.

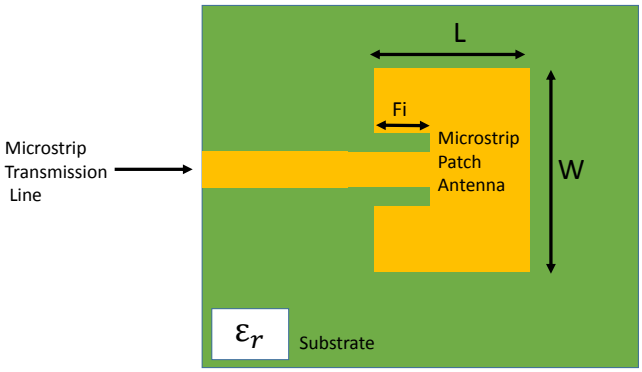

Figure 2.7: Top view of a microstrip patch antenna with an inset feed.

The width of the patch antenna is calculated by (2.34). Because the width has a small inverse relationship to the center resonant frequency, small changes to the width have little impact on the resonant frequency. Changes to the width have a greater effect on bandwidth. In order to understand the effect width has on the bandwidth of a patch antenna, refer to (2.35). It shows that if width increases and all other parameters remain the same, the bandwidth will increase directly.

$$W = \frac{1}{2f_r\sqrt{\mu_0\epsilon_0}}\sqrt{\frac{2}{\epsilon_r + 1}} \tag{2.34}$$

$$B \approx \frac{[\epsilon_r - 1]}{\epsilon_r^2}\frac{Wh}{L} \tag{2.35}$$

The input impedance of a patch antenna with this same orientation of transmission line feeding is typically within the range of 150 - 300 Ω. In order to reduce the input impedance for proper transmission line matching, the width of the antenna can be increased or an inset feed can be used. Keeping in mind the overall goal to create a less obtrusive antenna, an inset feed was used to keep the size of the patch antenna to a minimum. The input impedance of a rectangular antenna is needed in order to calculate the physical parameters of the inset feed. It is found using equations in 2.36 - 2.38, relating conductance (G) to resistance (R).

$$G_1 = \frac{-2 + cos(k_0W) + k_0W\int(\frac{sin(k_0W)}{k_0W})dW + \frac{sin(k_0W)}{k_0W}}{120\pi^2} \tag{2.36}$$

$$G_{12} = \frac{1}{120\pi^2}\int_0^\pi [\frac{sin(k_0Wcos(\theta))}{cos(\theta)}]J_0(k_0Lsin(\theta))sin^3(\theta)d\theta \tag{2.37}$$

$$R_{in} = \frac{1}{2(G_1 + G_{12})} \tag{2.38}$$

Fi, shown in fig. 2.7, can then be calculated using (2.39). The cut in the width direction of the patch antenna needs to be twice as wide as the transmission line that feeds the antenna. That means that there should be a cut that is half the width of the transmission line and Fi long on either side of the transmission line feeding the patch. This reduces the input impedance of the patch antenna because the input impedance of the patch decreases as the transmission line is attached closer to the center of the patch.

$$R_{feed} = R_{edge}cos^2(\frac{\pi Fi}{L}) \tag{2.39}$$

The length of the patch antenna directly relates to its center resonant frequency as calculated in (2.40) Analyzing this equation, it is seen that the length will be equal to half of the operating wavelength. Because the length of the patch is equal to $\frac{\lambda}{2}$ and the end of the patch antenna acts as an open circuited transmission line, there is a voltage maximum at the end of the patch and a voltage minimum at the beginning of the patch. This results in fringing electromagnetic fields.

$$f_c = \frac{c}{2L\sqrt{\epsilon_r}} = \frac{1}{2L\sqrt{\epsilon_0\epsilon_r\mu_0}} \tag{2.40}$$

In this model, fringing fields exist along the edge of the patch. They alter the electrical length of the patch antenna, meaning that the patch acts longer than it physically is. This change in effective length shifts the resonant center frequency of the patch antenna. The presence of fringing fields also implies that the electromagnetic waves propagate in the substrate in addition to in free space above the substrate. To account for this, an effective dielectric constant, ϵ_{eff}, is introduced. Accounting for these two things, (2.41) - (2.43) are used to calculate the corrected length of the antenna, which allows for the proper calculation of the center resonant frequency. Furthermore, the corrected wavelength for this model can be calculated using (2.44).

$$\epsilon_{eff} = \frac{\epsilon_r + 1}{2} + \frac{\epsilon_r - 1}{2[1 + 12\frac{h}{W}]^{0.5}} \tag{2.41}$$

$$\Delta L = 0.412H\frac{(\epsilon_{reff} + 0.3)(\frac{W}{h} + 0.264)}{(\epsilon_{eff} - 0.258)(\frac{W}{h} + 0.8)} \tag{2.42}$$

$$L = \frac{1}{2f_r\sqrt{\epsilon_{eff}}\sqrt{\mu_0\epsilon_0}} - 2\Delta L \tag{2.43}$$

$$\lambda = \frac{1}{f_r\sqrt{\epsilon_{eff}}\sqrt{\mu_0\epsilon_0}} \tag{2.44}$$

2.9 Antenna Arrays

When trying to deliver power over long distances, an antenna that is directive with a high amount of gain is beneficial. For this application, directional antennas and antenna arrays are used because they provide high directivity. A directional antenna focuses its energy and is positioned to aim the signal in a specific target direction. An antenna array is merely an assembly of single antenna elements that work together in order to deliver energy in a specific direction. This thesis project uses an antenna array with equally spaced elements placed in a straight line. This type of antenna array is called a Uniform Linear Array (ULA). The basic ULA configuration is shown in fig. 2.8 and is the basis of the configuration used in this thesis project. This antenna array works by feeding each of the antenna elements in parallel, but with different relative phases. The phase offset relative to adjacent elements allows energy to be focused in different directions. This technology outperforms an antenna that steers its energy by rotating the physical antenna because of the speed with which it can change its steering angle.

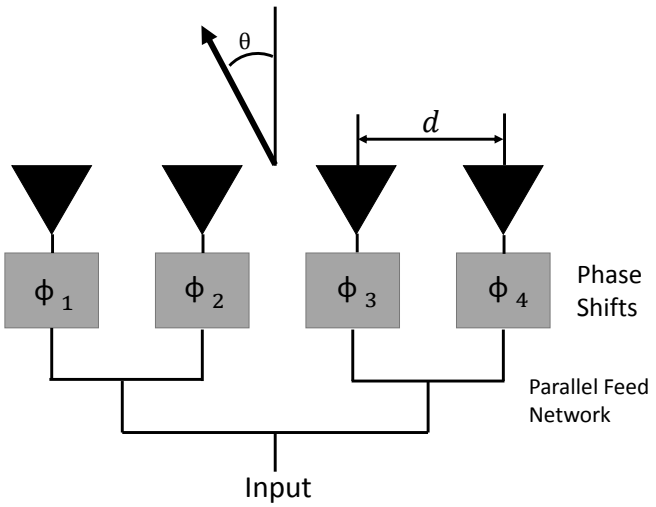

Figure 2.8: Configuration of ULA.

2.10 Analytic Software and Hardware

The software and hardware utilized to make this research possible were HFSS by ANSYS, MATLAB by MathWorks, a Vector Network Analyzer (VNA), and an Anechoic Chamber coupled with other Digital Asset Management Systems (DAMS) by Diamond Engineering. This section covers all contributing software and hardware in detail, explaining how the equipment functions and how it was used within this research.

2.10.1 High Frequency Structure Simulator (HFSS)

HFSS is used to simulate 3-D, full-wave, electromagnetic fields. Furthermore, it uses solver technologies based on finite element, integral equation, asymptotic and advanced hybrid methods to solve a wide range of micro-wave, RF, and high-speed digital applications. In the scope of this research, HFSS was used to design and simulate transmission lines and antennas. HFSS made it possible to understand the expected performance of the designs prior to physical construction, which saved time and provided data that was used to validate physical structure data.

2.10.2 MATLAB

MATLAB is a software used for analysis and design that operates on a platform designed specifically to solve engineering and scientific problems. For this research the MATLAB user friendly interface was used to do mathematical calculations on the simulated and experimental data. Once all mathematical manipulation were complete, the data was organized within MATLAB and was distilled into plots and graphs.

2.10.3 Vector Network Analyzer (VNA)

The VNA, shown in fig. 2.9, is an instrument that measures the port parameters within an electrical network. In this research the VNA was used to record the S-parameters from

fabricated antennas. The results from these measurements were used to compare simulated results in order to verify that resonance occurred at expected frequencies with expected gain values.

Figure 2.9: Vector Network Analyzer.

2.10.4 Anechoic Chamber

The anechoic chamber is a room designed to absorb reflections of sound and electromagnetic waves. This is done by covering the walls with pyramidal structures made of radiation absorbent material. Figure 2.10 shows what the room looks like with these structures attached to the walls, ceiling, and floor. These structures are designed to absorb incident RF radiation from as many incident directions as possible. The anechoic chamber is insulated from exterior sources of noise as it is within a Faraday cage. This allows for accurate data recording within the room by minimizing noise within the system. The anechoic chamber was accompanied by DAMS in this research in order to ensure accurate data recording when physical structures were tested.

2.10.5 Digital Antenna Measurement System (DAMS)

The DAMS comprises many different pieces of software and hardware. There is software used to manage all of the hardware, a signal generator, a horn antenna, an antenna positioner, and a network analyzer. For reference, fig. 2.11 shows a screen-shot of the DAMS interface.

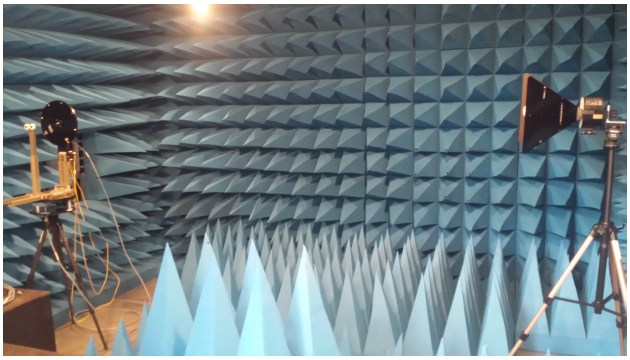

Figure 2.10: Anechoic Chamber.

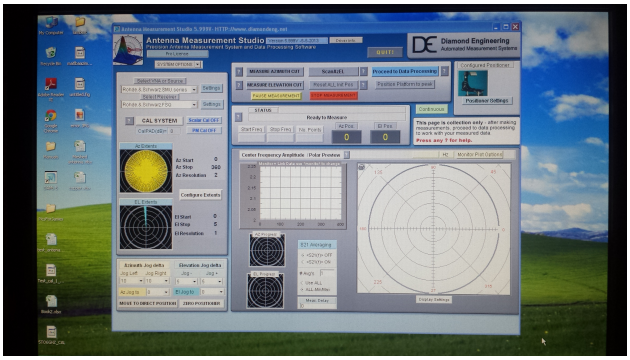

Figure 2.11: Antenna Measurement System Software.

The DAMS software interfaces with a signal generator to control the generated signal. This signal travels through a coaxial cable to a horn antenna, shown in fig. 2.12, which then transmits the signal within the anechoic chamber. The antenna positioner, shown in fig. 2.13, is used to orient the mounted antenna in specific directions. Once the antenna is oriented into a position, a network analyzer records the receiving signal strength. It then transfers that data to the DAMS software. The data then can be exported to an Excel spreadsheet for analysis. This system was used to measure the radiation pattern gain of an antenna. For this research, the fabricated antennas were tested using this process.

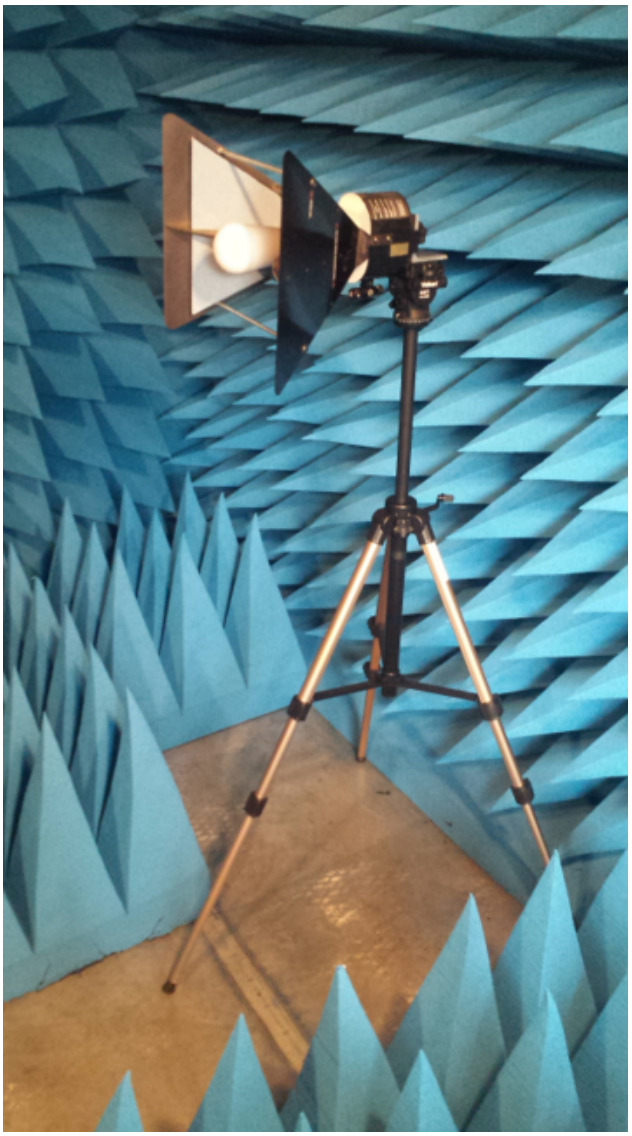

Figure 2.12: Horn Antenna used in Anechoic Chamber.

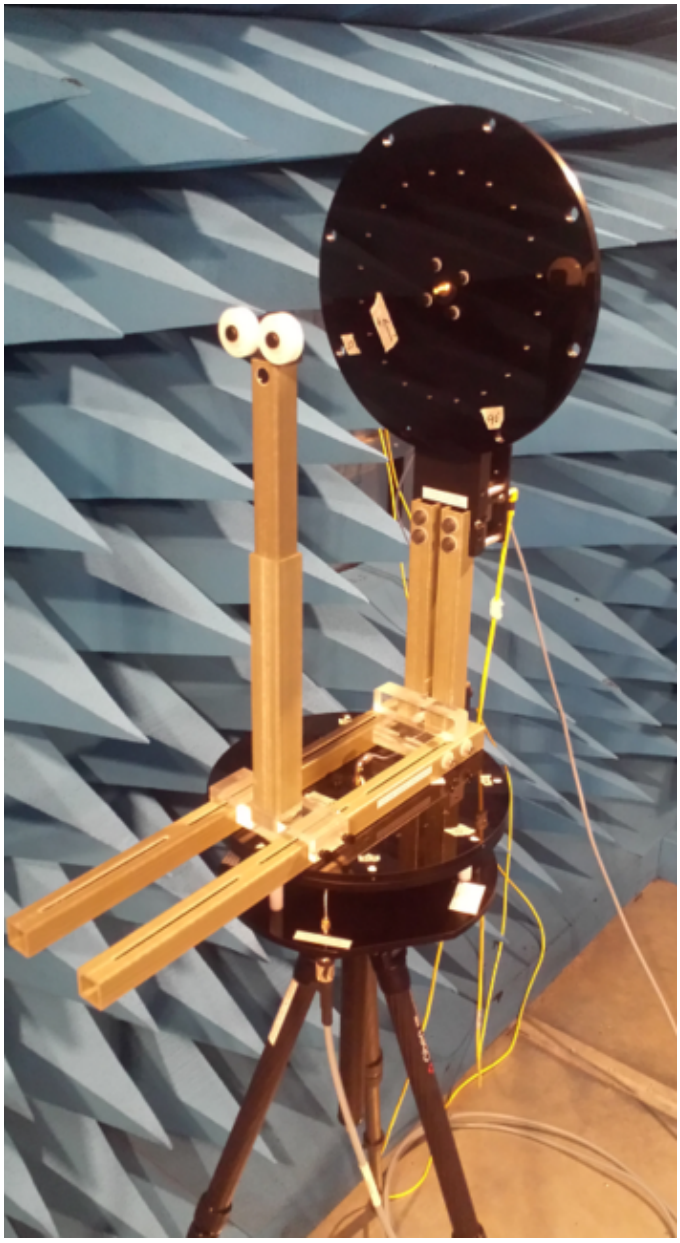

Figure 2.13: The Antenna Positioner

CHAPTER 3

Design of Vertically-Polarized and Horizontally-Polarized Antenna Systems

The contribution of this work is to present vertically-polarized and horizontally-polarized transparent directional antennas. Having both vertically and horizontally-polarized elements within the same antenna system enables the system to steer both horizontally and vertically. This feature makes the system highly desirable for window mount deployment, as the horizontal component of steering facilitates transmission to different buildings within the antennas range and the vertical component of steering facilitates transmission to the different floors of a building.

In order to fully evaluate the performance capabilities of the transparent hardware, equivalent opaque systems were designed and fabricated for comparison. Each antenna system required a phased feeding mechanism, or Butler matrix. The Butler matrix was designed to support specific beamsteering antenna functions. A control unit was designed and implemented to select multiple steering angles. This chapter describes the design and function of the phased feeding system and each of the antenna arrays.

3.1 Phased Feeding System

The phased feeding system was designed to support four steering angles, 22^o, -22^o, 7^o, and -7^o. In order to select one of the four steering angles, a two bit controller is implemented. Figure 3.1 shows the two bit controller. This two bit controller has three inputs: a data port (RFC), and two binary ports (A and B). It functions similarly to a demultiplexer with four

outputs, RF1, RF2, RF3, and RF4, each of which pertains to a different input to the Butler matrix. As the demultiplexer sends the data port signal to one of the four Butler matrix inputs, it simultaneously terminates the remaining output ports on the controller with 50 Ω terminations ensuring that the impedances are properly matched between the controller and the Butler matrix.

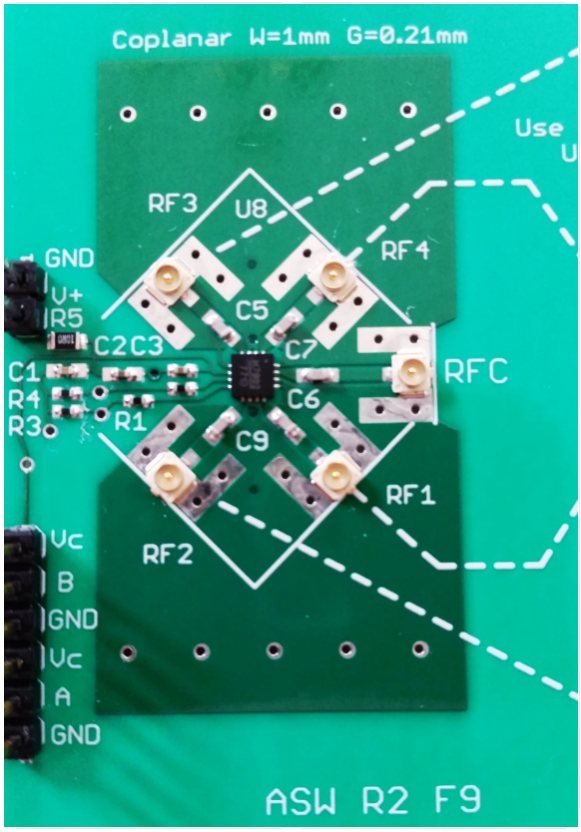

Figure 3.1: Two bit controller used to select one of four antenna steering angles.

Figure 3.2 shows the Butler matrix with the input ports on the left side and the output ports on the right side of the image. The two bit controller is connected to the Butler matrix input ports J-1, J-2, J-3, and J-4. The Butler matrix output ports are labeled as J-5, J-7, J-6, and J-8. It is important to note that the output pins are not in numerical order; J-6 and J-7 are flipped. This disorder at the output ports exist to support the function of the Butler matrix. This Butler matrix geometry renders specific phase delays required for proper antenna steering.

The Butler matrix uses couplers and phase delay components in order to deliver a signal to multiple output pins at different phases. The different output pins in this application drive four patch antennas. The excitation of each patch antenna at a different phase steers a beam at an angle (θ_s) in reference to boresight, or normal to the antenna array surface. This beam steering angle can be calculated using 3.1, where $\Delta\psi$ is the phase difference between adjacent outputs, d is the distance between adjacent antenna elements, θ_s is the steering angle, and λ is the wavelength of the frequency in which the system is operating.

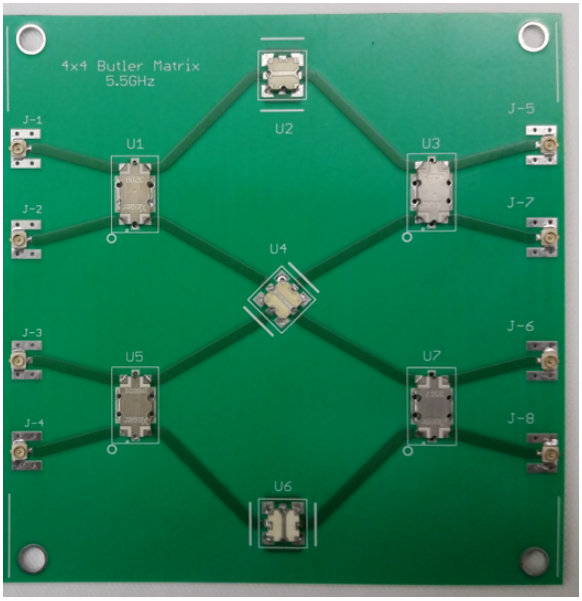

Figure 3.2: Butler matrix used to deliver a signal to multiple output pins at different relative phases.

$$\Delta\psi = \frac{360^o d sin(\theta_s)}{\lambda} \tag{3.1}$$

Simulations showed that adjacent patch antennas experience mutual coupling. In order to understand the magnitude of mutual coupling within an array as a function of element spacing, the antenna array was simulated with varying distance between elements. These simulations revealed that mutual coupling is negligible when the distance between antenna elements is greater than or equal to a wavelength. The analysis comparing different spacing of the antenna elements is covered later in this chapter.

As such, in order to meet size requirements without significant mutual coupling interference, each element within the array was spaced a wavelength apart. This reduces (3.1) to be simply (3.2).

$$\Delta\psi = 360^o sin(\theta_s) \tag{3.2}$$

Table 3.1: The relative phase at each of the four outputs of the Butler matrix corresponding to the binary input in the two bit control unit.

Binary Input	J-5	J-6	J-7	J-8	Steering Angle
00	0^o	135^o	270^o	405^o	22^o
01	0^o	-45^o	-90^o	-135^o	-7.18^o
10	0^o	45^o	90^o	135^o	7.18^o
11	0^o	-135^o	-270^o	-405^o	-22^o

The four different phase schemes and steering angles used in this research are shown in Table 3.1. In this table, the output J-5 of the Butler matrix is considered to be the 0^o phase reference and the other outputs are in reference to J-5. Furthermore, each binary input is shown in correspondence to each phase pattern.

3.2 Patch Antenna Elements

In order to construct a vertically-polarized and a horizontally-polarized antenna in the ULA configuration, individual elements with desired polarization must be developed. Previous work has been done on this project by others to develop a vertically-polarized antenna element. The design of this antenna can be seen in the research done by Escobar *et al.* [6], leaving only the design of a transparent horizontally-polarized patch antenna to be completed.

Figure 3.3a and 3.3b are the simulated evaluations of the horizontally-polarized patch element. This analysis was conducted to verify that the physical parameters in the simulations achieved the desired results. The S_{11} data, shown in fig. 3.3a, shows that the antenna is resonating at the desired frequency of 5.5 GHz. Figure 3.3b shows the azimuthal plane radiation plot of this element. The plot shows a gain of 6.62 dBi at boresight. The azimuthal plane radiation plot also shows a -3 dB beamwidth of 65^o, centered at 0^o. The directional shape of the plot is evidence that the patch is radiating properly. The final element parameters are provided in the next section.

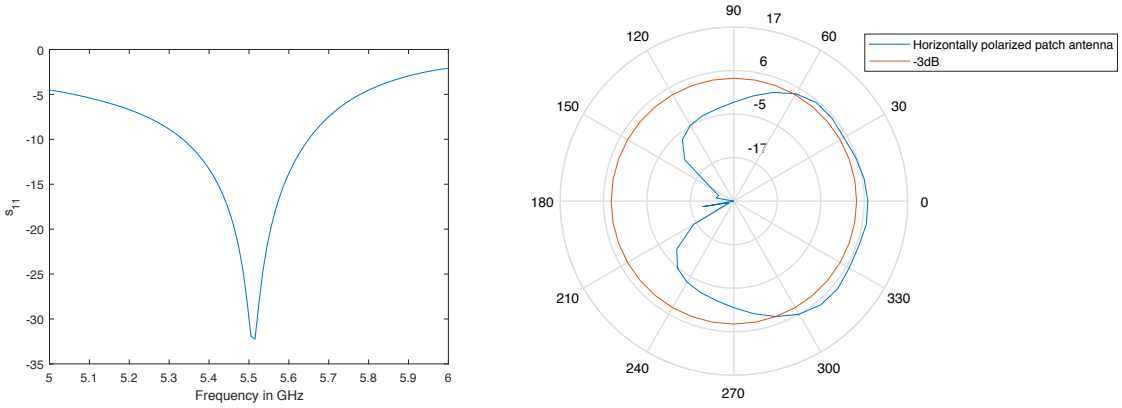

(a) Reflection Coefficient. (b) Electric field radiation pattern.

Figure 3.3: Horizontally-polarized patch antenna performance simulations.

Lastly, simulations were conducted in order to validate that both the vertically-polarized and horizontally-polarized antenna elements performed as expected in both opaque and transparent implementations. Figure 3.4 shows the S_{11} comparison of the single transparent and opaque vertically-polarized antennas and single transparent and opaque horizontally-polarized antennas using the HFSS simulator. As is shown, all four antennas are properly resonating at 5.5 GHz.

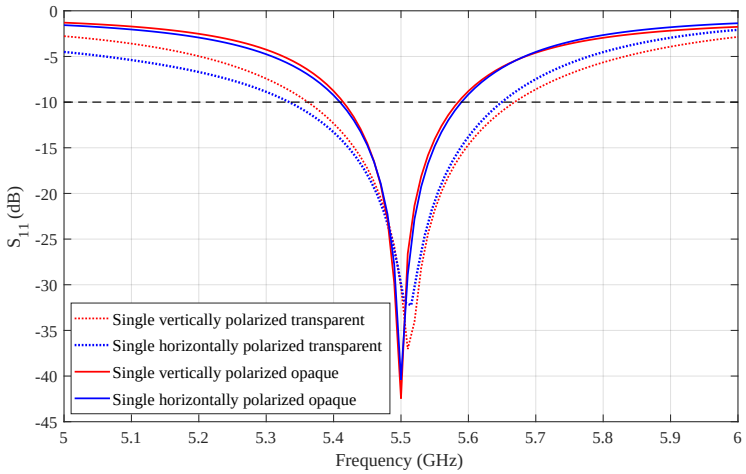

Figure 3.4: S_{11} of single transparent and opaque vertically-polarized antennas and single transparent and opaque horizontally-polarized antennas using the HFSS simulator.

Figure 3.5 shows the shape of the vertically-polarized patch antenna and Table 3.2 provides the dimensions associated with that figure. Figure 3.6 shows the shape of the horizontally-polarized patch antenna and Table 3.3 provides the dimensions associated with that figure. The performance of these elements is described in chapter 5.

Table 3.2: Dimensions used for the vertically-polarized patch antenna

Parameters	Opaque Vertical Patch (mm)	Transparent Vertical Patch (mm)
A	18.223	19.89
B	13.5	14.85
C	2.61	4.609
D	4.2	3.75
E	32.5	36.531
F	.85	2.109
G	1.9	5.346
H	8.426	8.316
I	3.5	8.02
J	32.5	34.06

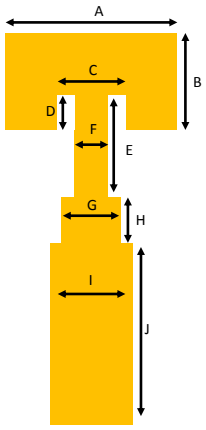

Figure 3.5: Defining dimensions of the vertical patch antenna, as given in Table 3.2.

Table 3.3: Dimensions used for the horizontally-polarized patch antenna

Parameters	Opaque Horizontal Patch (mm)	Transparent Horizontal Patch (mm)
A	18.223	19.89
B	13.5	14.85
C	2.61	4.609
D	4.2	3.75
E.a	8.476	9.26
E.b	32.5	32.807
F	.85	2.109
G	1.9	5.346
H	8.426	8.316
I	3.5	8.02
J	32.5	34.06

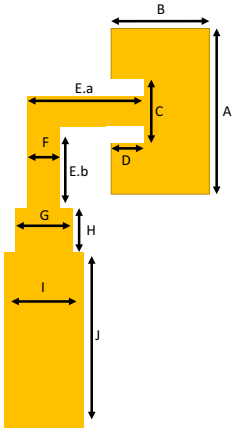

Figure 3.6: Defining dimensions of the horizontal patch antenna, as given in Table 3.3.

3.3 Patch Antenna Arrays

This section gives specifics on the individual antenna elements within each antenna array. There are four antennas in total: an opaque vertically-polarized antenna, an opaque horizontally-polarized antenna, a transparent vertically-polarized antenna, and a transparent horizontally-polarized antenna. The beginning of this section shows the physical parameters of each antenna. The end of this section shows the simulation analysis of parameters and array functions to verify that performance is as expected.

3.3.1 Array Parameter Specifics

The substrate for the opaque systems was 1.524 mm thick Rogers 4350B with a relative permittivity of 3.48. The substrate for the transparent systems was 2.93 mm thick Lexan with a relative permittivity of 2.8. Due to these dielectric differences in relative permittivity and thickness, the dimensions of the opaque and transparent patch antennas are slightly different, as they are optimized for the different materials. Furthermore, deriving the parameters for the opaque element used typical formulas for a patch antenna with a center resonant frequency of 5.5 GHz and 54.5 mm wavelength. Due to the thin wire mesh geometry, the dimensions for the transparent patch were rounded to the nearest mesh line, ensuring that each transparent element had a continuous conductive mesh perimeter.

An inset feed was used in both patch designs in order to match with a 100 Ω transmission line. Microstrip patch antennas typically have a high input impedance, but when using thin wire mesh material a lower characteristic impedance is desired. This is because at low characteristic impedances small changes in the number of mesh lines will not drastically change the feed line characteristic impedance [6]. The 100 Ω transmission line that is matched to the inset feed is connected to a quarter-wavelength transformer with a characteristic impedance of 70.7 Ω and then to a 50 Ω transmission line for impedance matching purposes within the network. Furthermore, the horizontally-polarized element has a 100 Ω feed line

that bends 90^o. Using the HFSS optimization tool, the length between the patch and the vertical transmission line was calculated to be one eighth of a wavelength.

The spacing between each element within an array is critical to performance. Most importantly, each element within the array must maintain high enough spatial diversity for beamsteering applications. In order to find the optimal element spacing that would support desired antenna steering angles, simulations were done in HFSS. The array used in this simulation is shown in fig. 3.7.

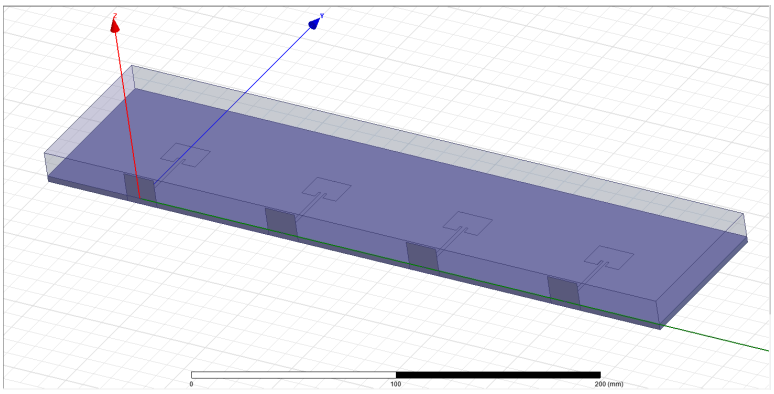

Figure 3.7: HFSS simulator view of vertically-polarized patch array.

In order to understand how element spacing affected the performance of the array, $\frac{\lambda}{2}$, λ, and $\frac{3\lambda}{2}$ spacings between each element performance were compared. The spacing of each element was measured as the distance between the centers of each feed port, not the nearest edge of radiating surfaces. Only the first and second antenna elements were tested in this simulation. Due to the symmetrical layout of the antenna, elements 2 and 3 are expected to behave identically, as are elements 1 and 4. A quick check was made to verify this, which held true. Referring to fig. 3.8 and 3.9 it is shown that there is no major difference between the λ and $\frac{3\lambda}{2}$ spacing, however, there is a difference between $\frac{\lambda}{2}$ and λ spacing. This provides evidence that at λ spacing and greater, the effects of mutual coupling diminish significantly.

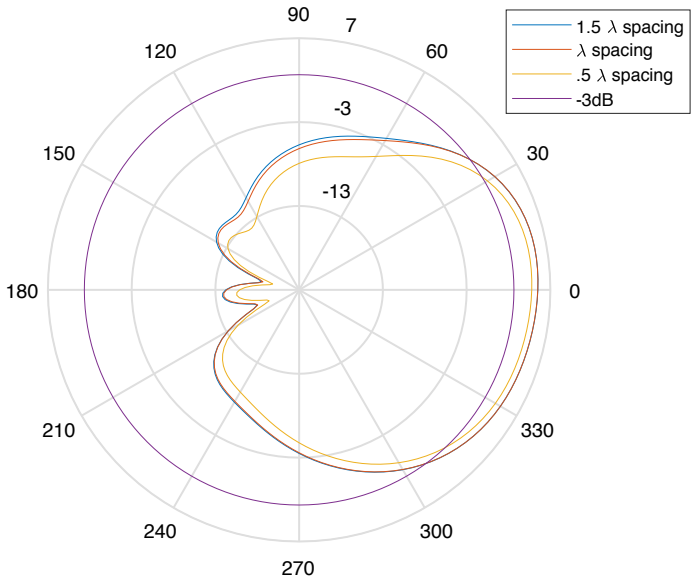

Figure 3.8: The electric field radiation plot of the first element in the array.

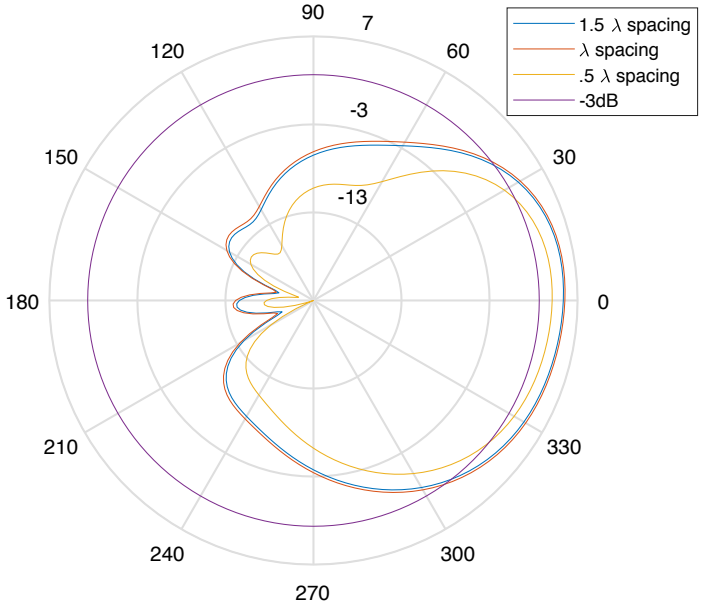

Figure 3.9: The electric field radiation plot of the second element in the array.

Table 3.4: Data from electric field radiation plots of first and second element spacing.

	Element 1 Beamwidth in Degrees	Element 2 Beamwidth in Degrees
$\frac{\lambda}{2}$	87.49	129.99
λ	95.01	142.49

As stated previously, one of the problems communications antennas face is how obtrusive they are. The size of hardware is a major factor. For this reason, taking into account simulation results, the individual element spacing within the arrays was chosen to be a wavelength as it is the smallest distance between each element that limits the effects of mutual coupling.

The ground plane size of each antenna must be large enough in order to emulate an infinite ground plane. The final experimental ground plane of the opaque antennas was 117.475 mm tall and 234.95 mm wide, while that of the transparent antennas were 215.9 mm tall and 298.45 mm wide. The size difference between the two is due to extra components in the transparent hardware such as the edge board, which is explained more in Chapter 4.

3.3.2 Simulations of the Arrays

This section presents electric field radiation plots of both the vertically and horizontally-polarized antenna arrays, given the antenna parameters provided in the previous section. Figure 3.10a shows the horizontally-polarized array's azimuthal plane radiation pattern at boresight, where the main lobe is centered at 0^o as expected. Figure 3.10b shows the same array's azimuthal plane radiation pattern when steered to 22^o. The main lobe of this plot is centered at 22^o as desired. Furthermore, the symmetry in these azimuthal plane radiation plots is due to the physical symmetry of the antenna array.

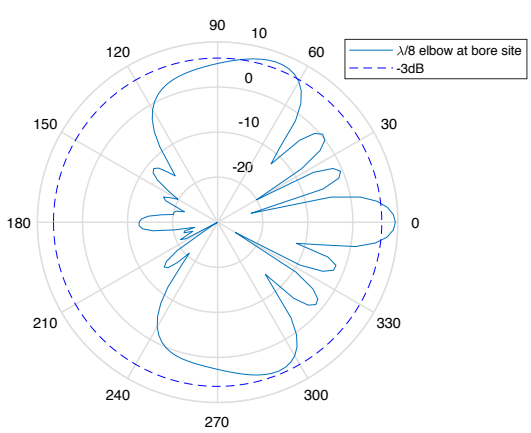

(a) Steered to boresight.

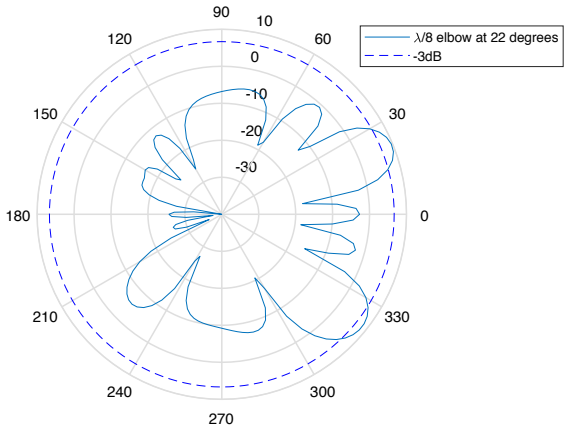

(b) Steered to 22^o.

Figure 3.10: Azimuthal plane radiation pattern of horizontally-polarized array.

Figure 3.11a shows the vertically-polarized array elevation plane radiation pattern when steered to boresight. The main lobe of this plot is centered at 0^o as expected. Figure 3.11b shows the same array's elevation plane radiation pattern steered to 22^o, where the main lobe of this plot is centered at 22^o as desired. The symmetry in the elevation plane radiation plot seen in this figure is again due to the physical symmetry of the antenna array.

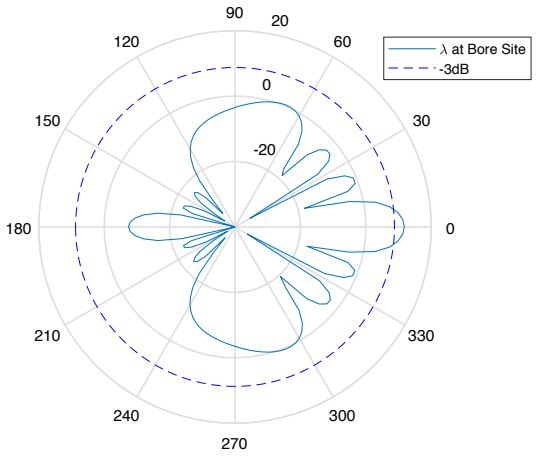

(a) Steered to boresight.

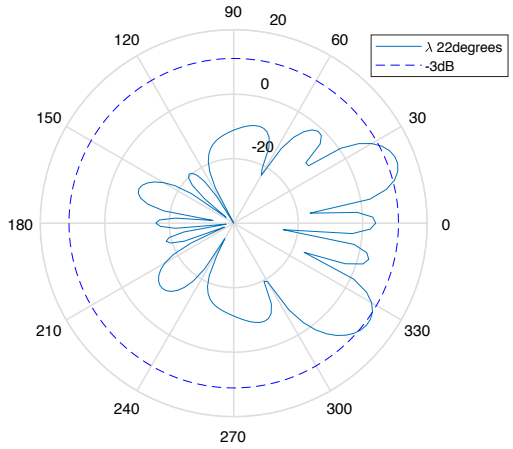

(b) Steered to 22^o.

Figure 3.11: Elevation plane radiation pattern of vertically-polarized array.

3.3.3 System Setup

Figure 3.12 is a block diagram showing how each of the components in this system is connected. The two bit control unit must be connected to the 4x4 Butler matrix as indicated because the function of the Butler matrix is specific to which input port the RF power is delivered. J-6 and J-7 outputs of the Butler matrix must be crossed over when connected to antenna elements so that the phase difference between each adjacent pair of antenna elements is constant. This phase difference is crucial in supporting the four steering functions of the system.

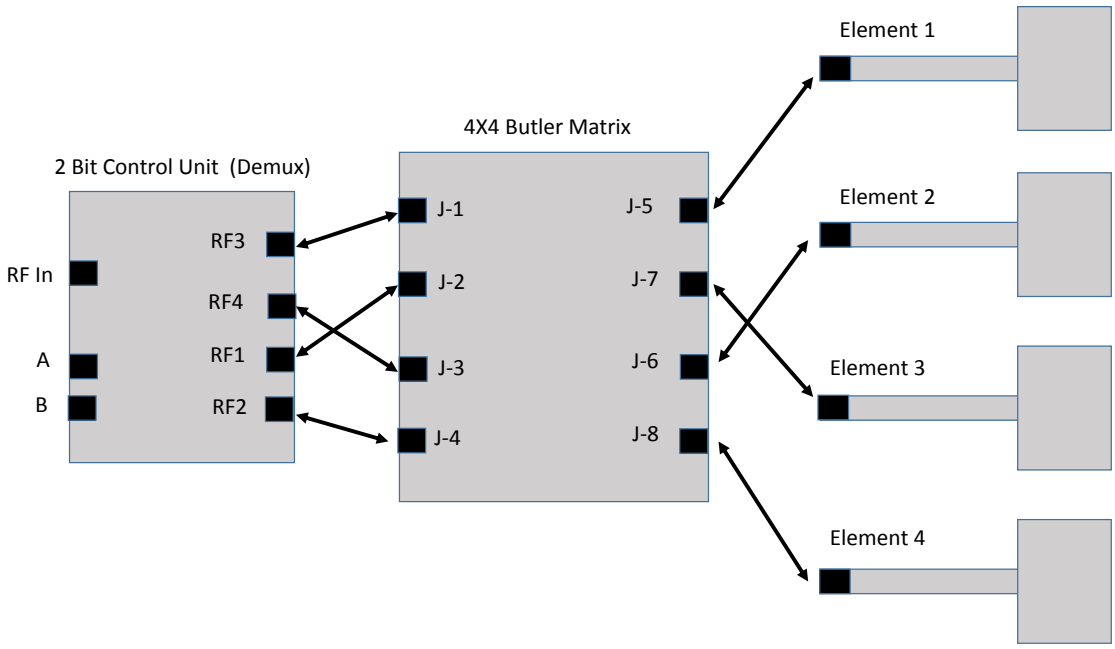

Figure 3.12: Diagram of a complete antenna system.

CHAPTER 4

Fabrication

The fabrication process for the opaque and transparent antenna systems is very important to the outcome of this thesis project because the accuracy with which a physical model is built affects the measurements recorded from that component. If the results from simulation and the physical model differ greatly, it is due to either A) simulations of the design were flawed, or B) the physical model was fabricated incorrectly. Thus, in order to validate the simulations, it is extremely important to fabricate the physical models precisely. The following chapter covers each step of the fabrication process for the opaque and transparent systems.

4.1 Opaque Hardware

The components of the opaque systems in this project that required printed circuit board (PCB) fabrication were the two bit controller, the Butler matrix, the vertically-polarized opaque patch antennas, and the horizontally-polarized opaque patch antennas. The component of the transparent systems in this project that required PCB fabrication was the edge board. To facilitate fabrication, the designs of the PCB components were exported from simulation software and were outsourced to the company Advanced Circuits of 4PCB.com.

Figure 4.1 shows the PCB that contains both the two bit control unit (left side of image) and the Butler matrix (right side of image). These two circuits are connected with UMCC cables; the overall board dimensions are 152.4 mm wide by 95.25 mm tall.

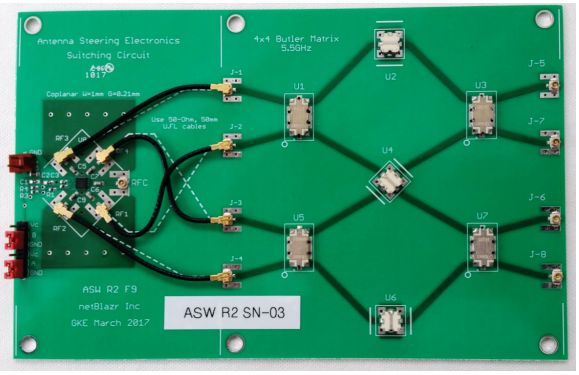

Figure 4.1: Fabricated two bit control unit (left) and Butler matrix (right) on same PCB.

Figure 4.2 shows the PCB that is used to connect the Butler matrix to transparent microstrip transmission lines. As in fig. 4.2, there are five holes drilled in the edge board to allow the edge board to be mounted onto the Lexan dielectric. The edge board mounting is explained in more depth in Appendix A. The edge board, measuring 222.25 mm long by 1.905 mm tall, uses UMCC connectors to connect to the Butler matrix.

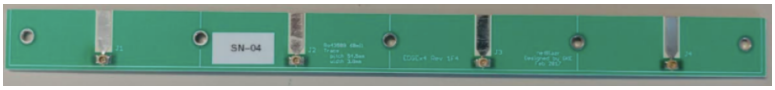

Figure 4.2: Edge board used to electrically connect transparent hardware to Butler matrix with UMCC connectors.

Figures 4.3a and 4.3b show the vertically-polarized antenna array and the horizontally-polarized antenna array respectively. Both systems measure 234.95 mm long by 117.475 mm tall. Theses antennas were connected to a mounting chassis in order to facilitate measurements within the anechoic chamber. Figure 4.4 shows the opaque antenna array (right) and the steering hardware (center) attached to the antenna positioner (left).

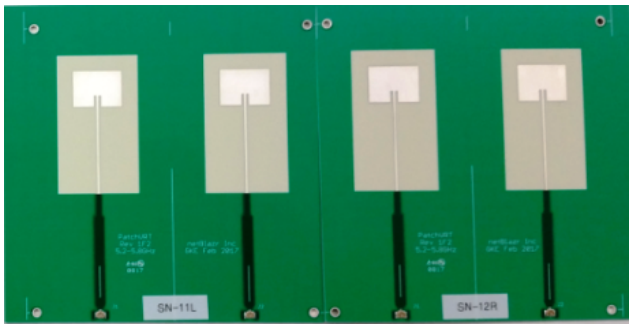

(a) Vertically-polarized opaque antenna array.

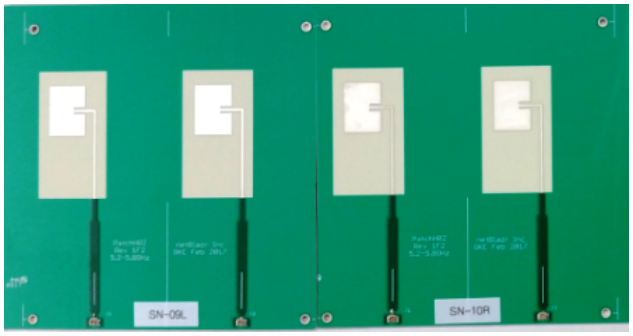

(b) Horizontally-polarized opaque antenna array.

Figure 4.3: Opaque antenna arrays.

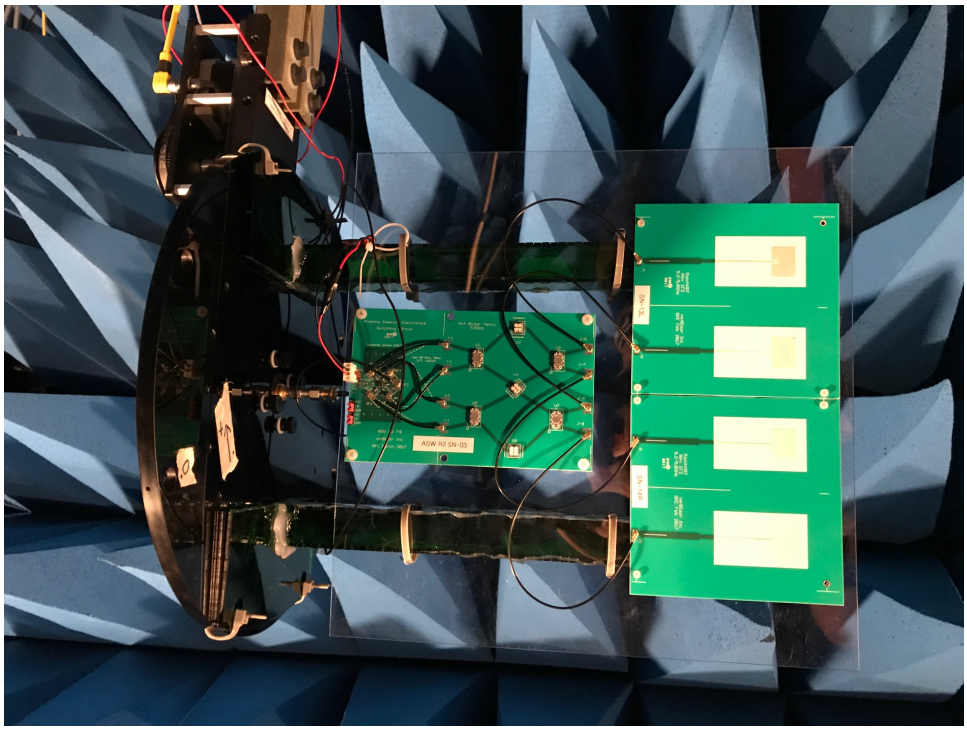

Figure 4.4: Opaque antenna array (right), with steering hardware (center), attached to the antenna positioner (left) in the anechoic chamber.

4.2 Transparent Antennas

The fabrication of the transparent antennas required a specific cutting process in order to maintain a conductive strip along the transparent antenna perimeters. A laser cutting machine with image recognition and an error tolerance on the magnitude of nanometers was required due to the size of the mesh wires within the mesh material. Photo Machining Inc. of Pelham, NH was contracted to perform this work with a picosecond laser. Appendix A presents a step by step procedure for how the transparent antenna was fabricated.

Figure 4.5 is a picture of the transparent vertically-polarized antenna array as fabricated. Figure 4.6 is a picture of the transparent horizontally-polarized antenna array as fabricated.

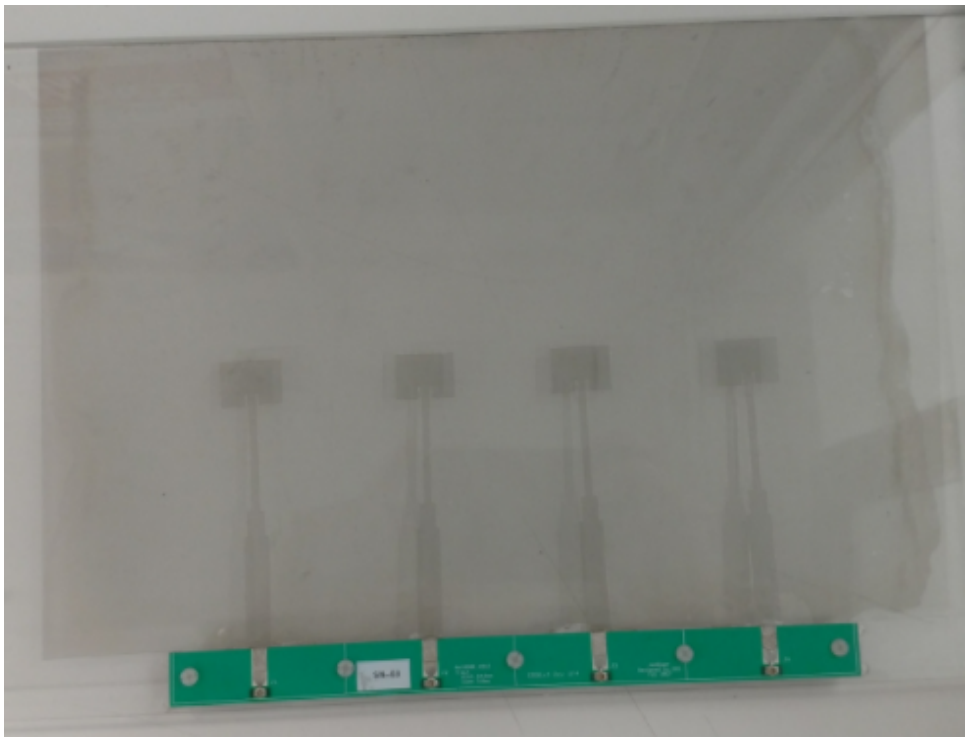

Figure 4.5: Vertically-polarized transparent antenna array.

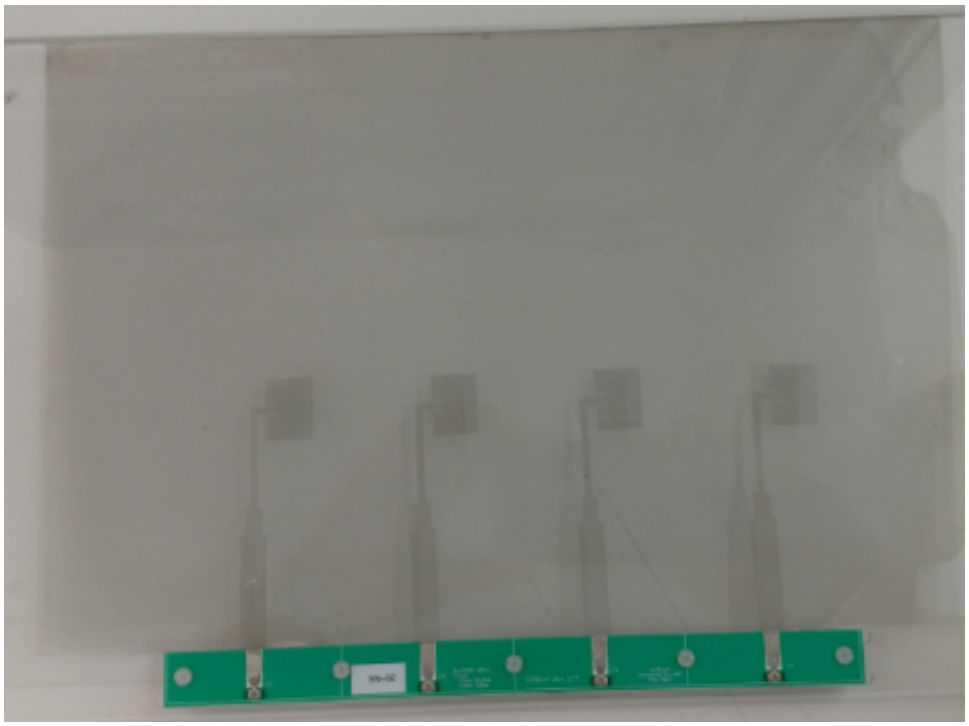

Figure 4.6: Horizontally-polarized transparent antenna array.

CHAPTER 5

Empirical Results

In this chapter, the performance of the following components is presented: steering hardware, the individual elements within each array, the opaque and transparent vertically-polarized antenna, and the opaque and transparent horizontally-polarized antenna. The contribution of this work is the demonstration of both vertically and horizontally-polarized steerable transparent antennas. Pictures of both fabricated antennas can be seen in Appendix B.

5.1 Steering Hardware

Table 5.1 shows the measured relative phase angles with J-5 port as reference of the fabricated Butler matrix and two bit control unit. Compared to the theoretical values in Table 3.2, the measured values differ slightly, but were capable of supporting the four steering angles. The table shows that the two bit controller is able to switch between four different phase schemes. At this point, the performance of the two bit controller and the Butler matrix was validated and the components are implemented within the antenna systems without fault.

Table 5.1: Measured relative phases at each output of the Butler matrix corresponding to each of the four binary inputs to the control unit.

Binary Input	J-5	J-6	J-7	J-8
00	0^o	141.86^o	281.97^o	399.64^o
01	0^o	-57.95^o	-90.58^o	-147.96^o
10	0^o	39.95^o	87.78^o	135.01^o
11	0^o	-145.92^o	-274.9^o	-416.6^o

5.2 Performance Analysis of Individual Elements within Antenna Arrays

The performance of the individual antenna elements is crucial for the overall array to function properly. This section presents the performance of the individual vertically-polarized and horizontally-polarized antenna elements as they operate within the array. The analysis of the individual antenna elements is presented in order to understand the performance of antenna elements within an antenna array, as their performance may differ from isolated cases. 50 Ω terminations were applied to the unused elements in these individual element measurements.

5.2.1 Reflection Coefficient of Vertically-Polarized Antenna Elements

This section compares the simulated and measured reflection coefficients for each of the four vertically-polarized elements within the opaque and transparent vertically-polarized antenna arrays. Figures 5.1a-5.1d pertain to the first element through the fourth element in an array, respectively.

Figure 5.1a shows that the simulated opaque element has a -10 dB return loss bandwidth of 6.36% centered at 5.5 GHz while the measured opaque element bandwidth is 4.5% centered at 5.5 GHZ. The simulated transparent element has a bandwidth of 4.9% centered at 5.5 GHz while the measured transparent element bandwidth is 5.9% centered at 5.65 GHz.

Figure 5.1b shows that the simulated opaque element has a -10 dB return loss bandwidth of 6.4% centered at 5.5 GHz while the measured opaque element bandwidth is 2.2% centered at 5.5 GHZ. The simulated transparent element has a bandwidth of 2.2% centered at 5.5 GHz while the measured transparent element bandwidth is 5.3% centered at 5.76 GHz.

Figure 5.1c shows that the simulated opaque element has a -10 dB return loss bandwidth of 5.9% centered at 5.5 GHz while the measured opaque element bandwidth is 2.2% centered at 5.5 GHZ. The simulated transparent element has a bandwidth of 2.7% centered at 5.5 GHz while the measured transparent element bandwidth is 2.7% centered at 5.88 GHz.

Figure 5.1d shows that the simulated opaque element has a -10 dB return loss bandwidth of 6.7% centered at 5.5 GHz while the measured opaque element bandwidth is 4.7% centered at 5.5 GHZ. The simulated transparent element has a bandwidth of 2.5% centered at 5.5 GHz while the measured transparent element bandwidth is 6.4% centered at 5.75 GHz.

The transparent antennas have different ground planes and substrates than the opaque antennas, which was expected to cause a slight difference in resonant frequencies. Furthermore, the shift in resonant frequency for transparent elements could be due to variations in patch antenna length caused by the discrete mesh lines of the mesh conductor, or the result of errors within the fabrication process.

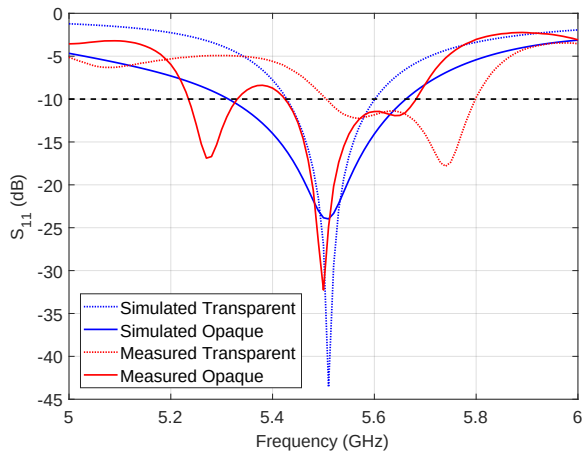

(a) First element in the array.

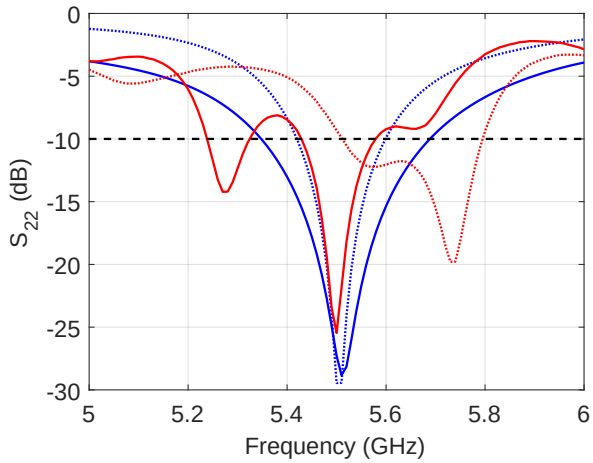

(b) Second element in the array.

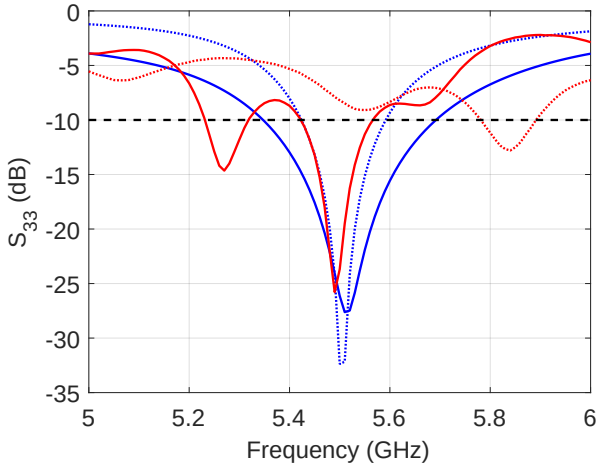

(c) Third element in the array.

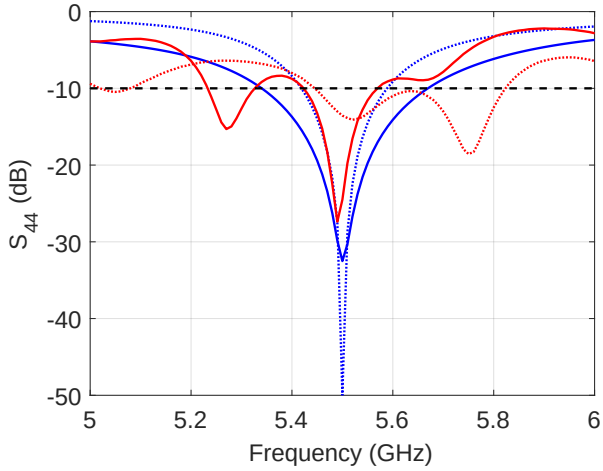

(d) Fourth element in the array.

Figure 5.1: The S_{11} plots of each of the elements within each of the vertically-polarized arrays.

5.2.2 Reflection Coefficient of Horizontally-Polarized Antenna Elements

This section compares the simulated and measured reflection coefficients for each of the four horizontally-polarized elements within the opaque and transparent horizontally-polarized antenna arrays. Figures 5.2a-5.2d pertain to the first element through the fourth element in an array respectively.

Figure 5.2a shows that the simulated opaque element has a -10dB return loss bandwidth of 3.9% centered at 5.5 GHz while the measured opaque element bandwidth is 1.6% centered

at 5.48 GHZ. The simulated transparent element has a bandwidth of 4.9% centered at 5.5 GHz while the measured transparent element bandwidth is 3.87% centered at 5.6 GHz.

Figure 5.2b shows that the simulated opaque element has a -10dB return loss bandwidth of 3.2% centered at 5.5 GHz while the measured opaque element bandwidth is 8% centered at 5.5 GHZ. The simulated transparent element has a bandwidth of 7% centered at 5.45 GHz while the measured transparent element bandwidth is 6% centered at 5.75 GHz.

Figure 5.2c shows that the simulated opaque element has a -10dB return loss bandwidth of 10% centered at 5.5 GHz while the measured opaque element bandwidth is 4.7% centered at 5.5 GHZ. The simulated transparent element has a bandwidth of 6.4% centered at 5.45 GHz while the measured transparent element bandwidth is 6% centered at 5.75 GHz.

Figure 5.1d shows that the simulated opaque element has a -10dB return loss bandwidth of 7.2% centered at 5.5 GHz while the measured opaque element bandwidth is 2.7% centered at 5.5 GHZ. The simulated transparent element has a bandwidth of 6% centered at 5.45 GHz while the measured transparent element bandwidth is 5.3% centered at 5.72 GHz.

The lack of a sharp resonance for horizontally-polarized patches can be attributed to an impedance mismatch caused by the 90^o turn in the transmission line. The transparent antennas have different ground planes and substrates than the opaque antennas, which was expected to cause a slight difference in resonant frequencies. Furthermore, the shift in resonant frequency for transparent elements could be due to variations in patch antenna length caused by the discrete mesh lines of the mesh conductor, or the result of errors within the fabrication process.

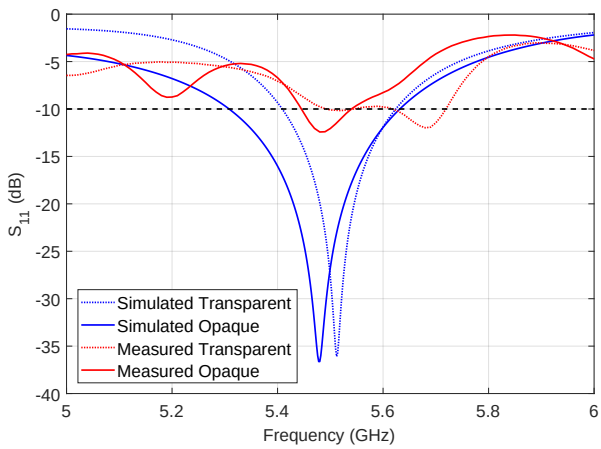

(a) First element in the array.

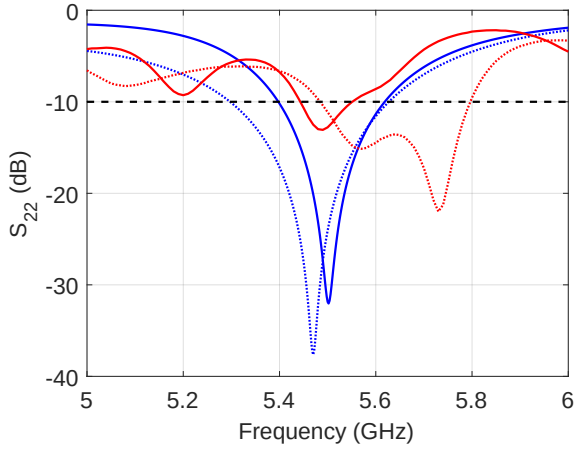

(b) Second element in the array.

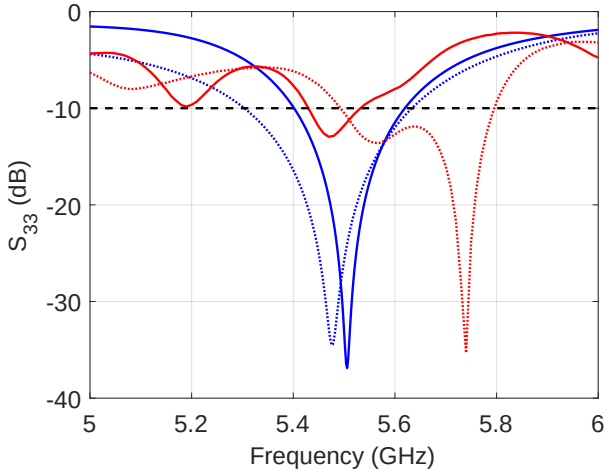

(c) Third element in the array.

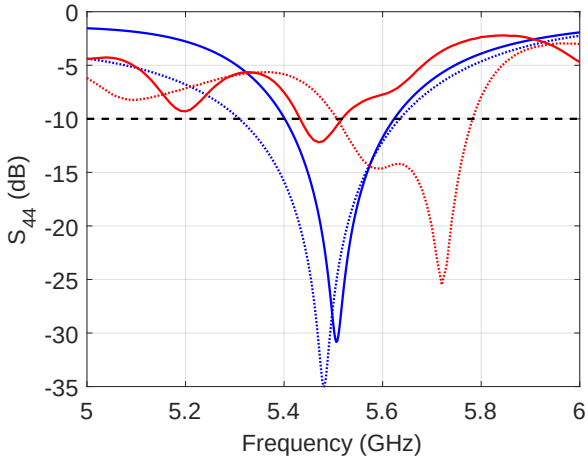

(d) Fourth element in the array.

Figure 5.2: The S_{11} plots of each of the elements within each of the horizontally-polarized arrays.

5.2.3 Elevation Plane Radiation Pattern of Vertically-Polarized Antenna Elements

Figures 5.3a-5.3d show the elevation plane radiation pattern for all of the vertically-polarized antenna elements. All simulated plots for opaque and transparent elements have a maximum gain between 6 and 8 dBi while all measured plots for both opaque and transparent elements have a maximum gain between 6 and 7.2 dBi. The difference between the maximum gain of the measured transparent elements and that of the measured opaque elements doesn't exceed 1.2 dB, which concur with research done by Escobar *et al.* [2] [6]. All elevation plane radiation patterns of vertically-polarized antenna elements show no signs of

mutual coupling between elements. 50 Ω terminations were applied to the unused elements in these individual element measurements.

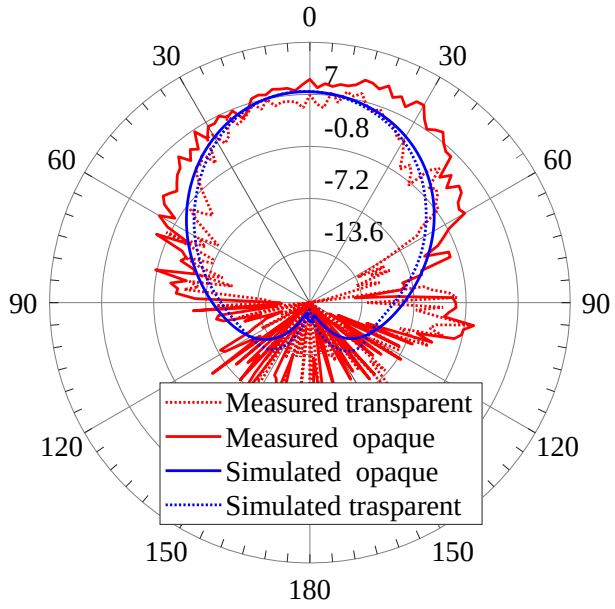

(a) First element in the array.

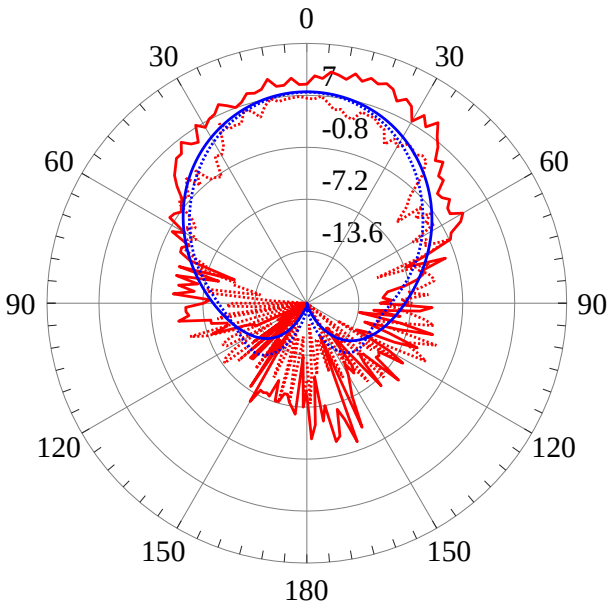

(b) Second element in the array.

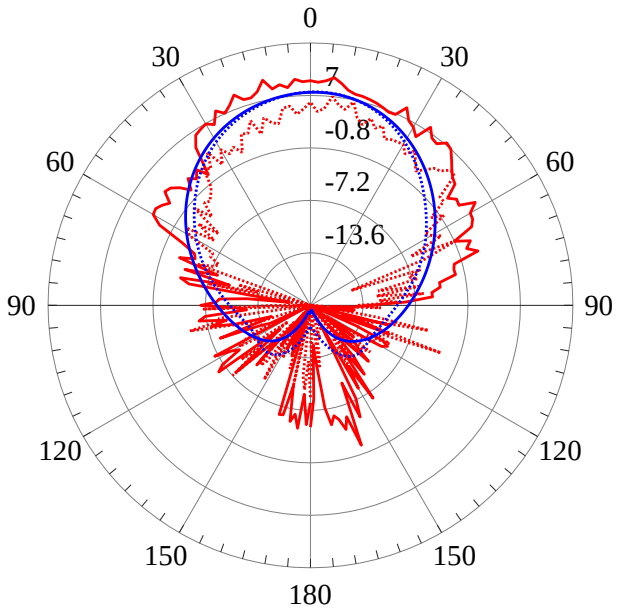

(c) Third element in the array.

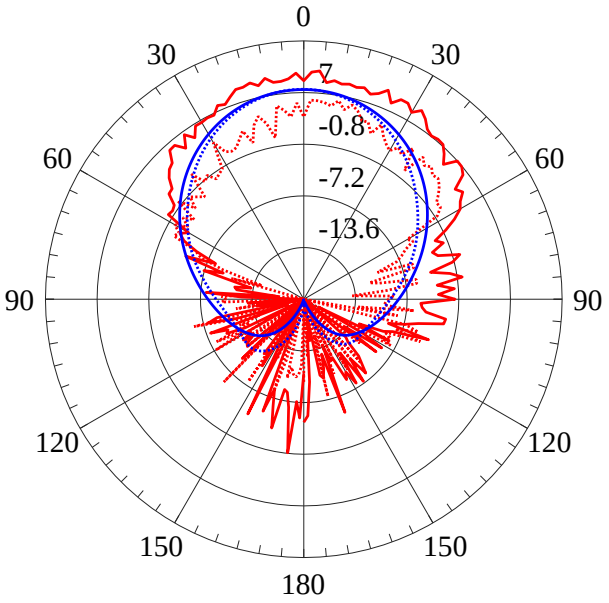

(d) Fourth element in array.

Figure 5.3: The elevation plane radiation plots of the four elements within each of the vertically-polarized arrays.

5.2.4 Azimuthal Plane Radiation Pattern of Horizontally-Polarized Antenna Elements

Figures 5.4a-5.4d show the azimuthal plane radiation pattern for all the horizontally-polarized antenna elements. All simulated plots for opaque and transparent elements have a maximum gain between 6 and 8 dBi. Furthermore, all measured plots for both opaque and transparent elements have a maximum gain between 6 and 7.2 dBi. The difference between the maximum gain of the measured transparent elements and the measured opaque elements doesn't exceed 1.2 dB, which concur with research done by Escobar *et al.* [2] [6]. As with the vertically-polarized antenna elements, the radiation patterns of the horizontally-polarized antenna elements show no signs of mutual coupling between elements. 50 Ω terminations were applied to the unused elements in these individual element measurements.

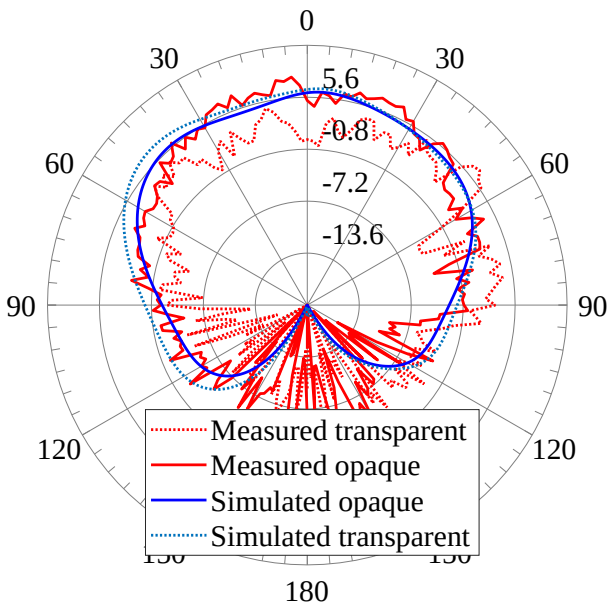

(a) First element in the array.

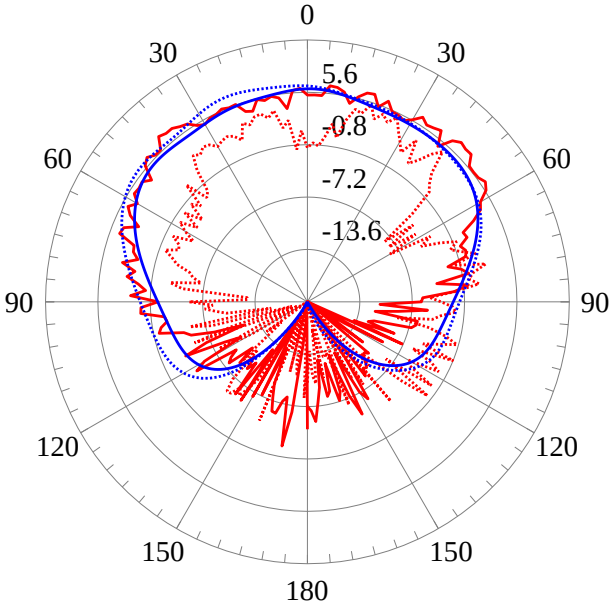

(b) Second element in the array.

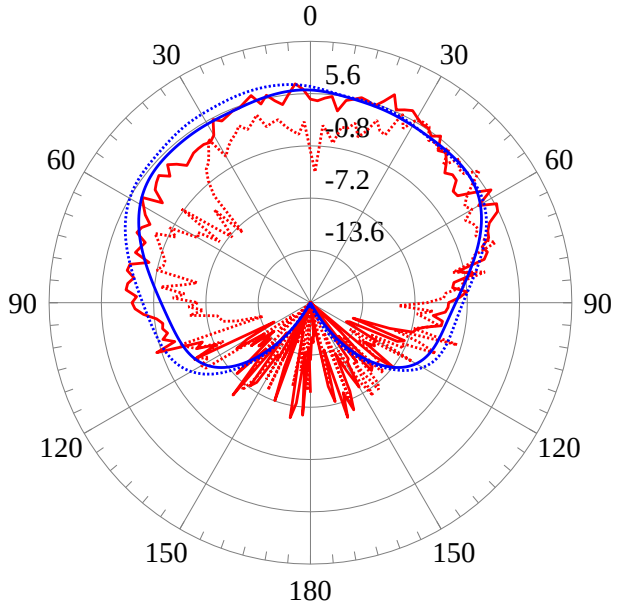

(c) Third element in the array.

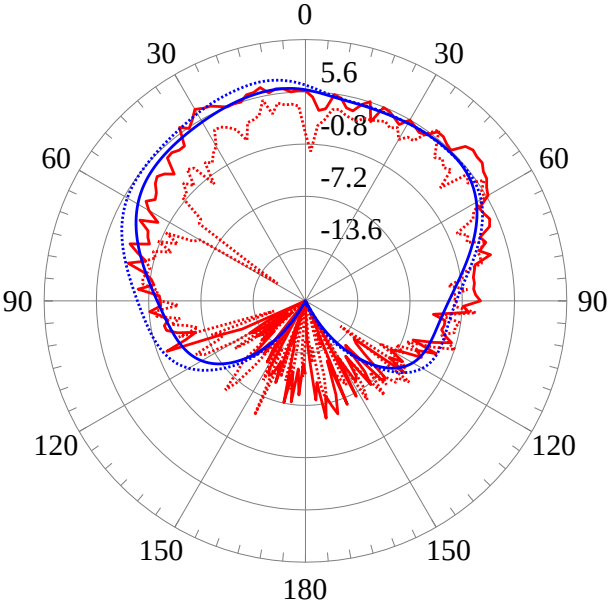

(d) Fourth element in the array.

Figure 5.4: The azimuthal plane radiation plots of the four elements within each of the horizontally-polarized arrays.

5.3 Vertically-Polarized Array

Table 5.2 shows the resulting values from the HFSS simulations and the physical experiments performed on the vertically-polarized array. The physical experiments were performed in an anechoic chamber through the use of DAMS. The data shows that the simulated transparent array and the simulated opaque array operated similarly. It is important to note that these simulations were made using design-specified phase excitations for each of the array elements, which are presented in Table 3.1.

The measured transparent and opaque arrays operate very similarly. At the 7^o and -7^o steering angles, the vertically-polarized transparent array has a gain roughly 2 dB lower than the opaque array. At the 22^o and -22^o steering angles, the vertically-polarized transparent array has a gain roughly 3 dB lower than the opaque array.

Figures 5.5-5.8 show elevation plane radiation plots comparing the performance of the simulated and measured transparent and opaque vertically-polarized patch antennas. The elevation plane radiation plots of binary inputs 00 and 11, fig. 5.5 and fig. 5.6 respectively, are very similar due to the physical symmetry of the arrays and the symmetry of the phase excitations. The same comparison can be seen between the radiation plots for binary inputs 01 and 10, fig. 5.7 and fig. 5.8 respectively. The main lobe -3 dB beamwidths of all vertically-polarized antennas, both simulated and measured, are alike, producing beamwidths of 12^o to 16^o. The measured steering angle of each plot was defined as the center of each main lobe. The tolerance range is defined as the -3 dB beamwidth of the main lobe. Both the measured and simulated steering angles, similar to each other, fall within this range, proving that the antenna is successfully steered to that angle.

Table 5.2: Vertically-Polarized Patch Antennas

Binary Input	Antenna	Max Gain (dBi)	Steering Angle (Degrees)	Beamwidth (Degrees)
00	Simulated Transparent	10.4	21^o	14^o
00	Simulated Opaque	10.4	21.5^o	13^o
00	Measured Transparent	4.7	23^o	16^o
00	Measured Opaque	8.0	28^o	14^o
01	Simulated Transparent	11.8	-7^o	12^o
01	Simulated Opaque	11.6	-7^o	12^o
01	Measured Transparent	6.5	-9^o	12^o
01	Measured Opaque	8.7	-2^o	14^o
10	Simulated Transparent	11.8	7^o	12^o
10	Simulated Opaque	11.6	7^o	12^o
10	Measured Transparent	6.9	1^o	12^o
10	Measured Opaque	8.8	12^o	13^o
11	Simulated Transparent	10.4	-21^o	14^o
11	Simulated Opaque	10.5	-21^o	14^o
11	Measured Transparent	5.2	-25^o	12^o
11	Measured Opaque	8.0	-18^o	14^o

Figure B.1 is a picture of the transparent vertically-polarized array installed on an office window. As shown, the antenna array allows for natural light to pass through the window and obstructs the view from the window much less than an opaque antenna would. This satisfies the design specification for transparency of the antenna.

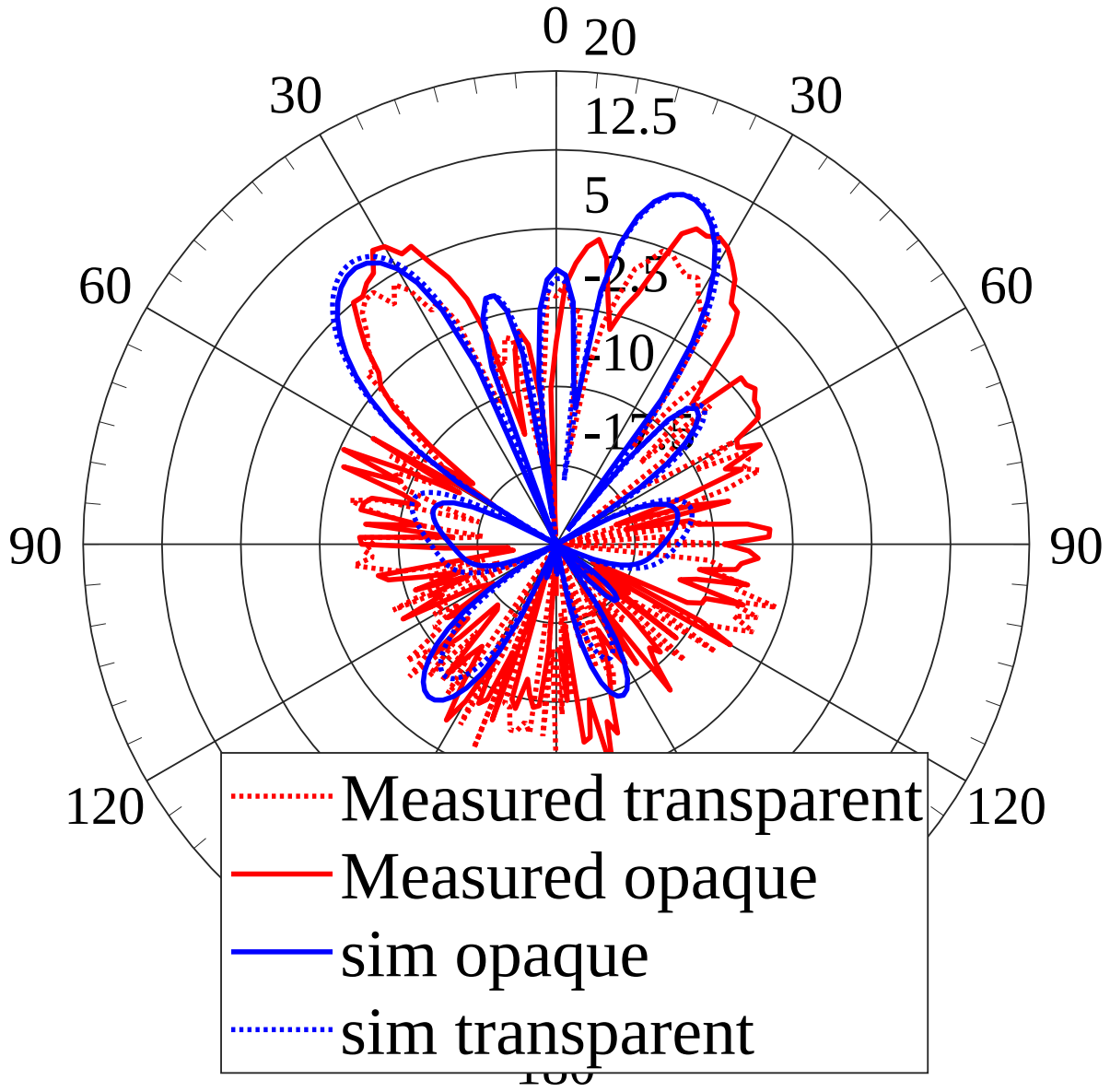

Figure 5.5: Vertically-polarized array with binary input 00, resulting in a 22^o steering angle.

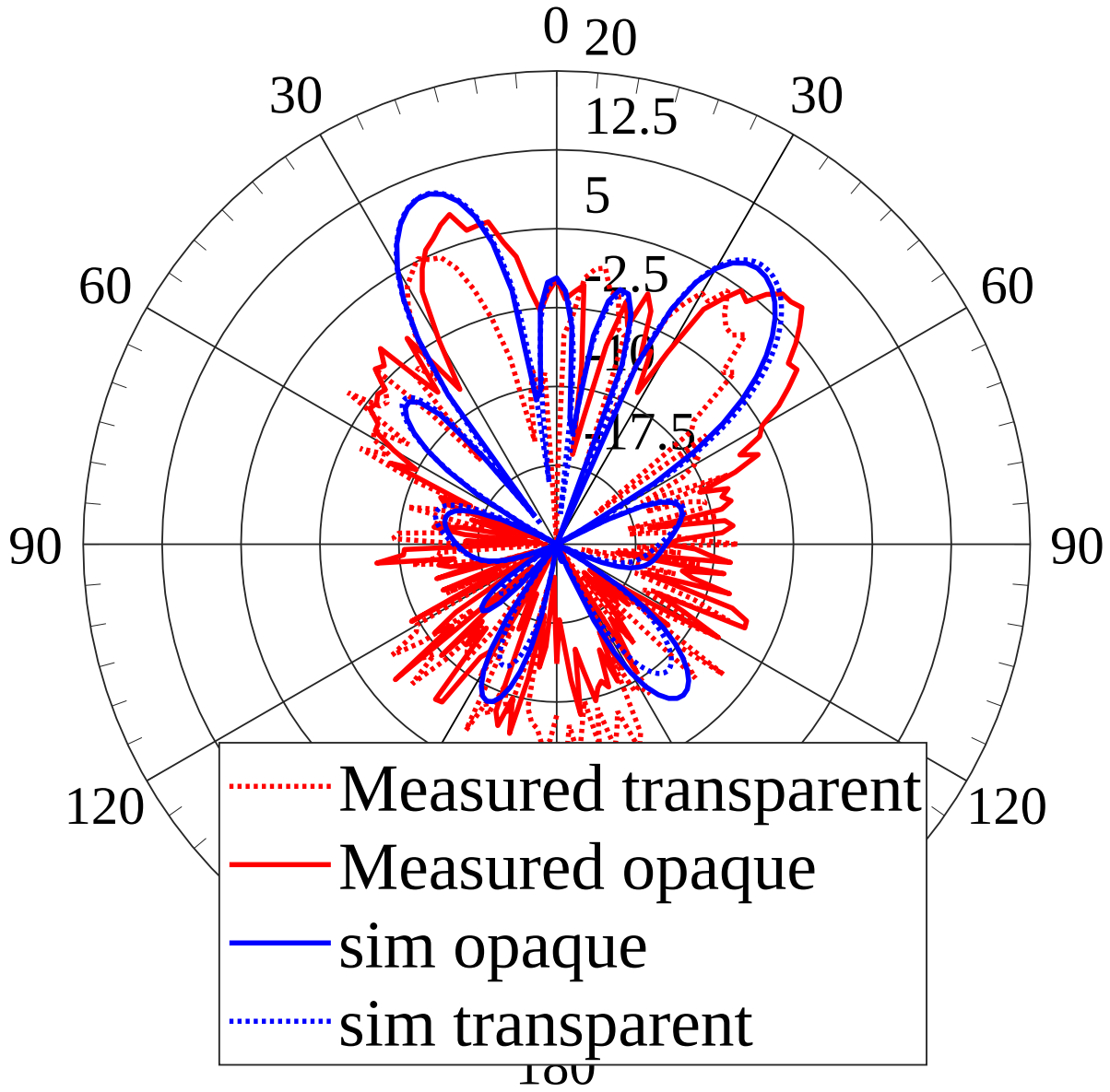

Figure 5.6: Vertically-polarized array with binary input 11, resulting in a -22^o steering angle.

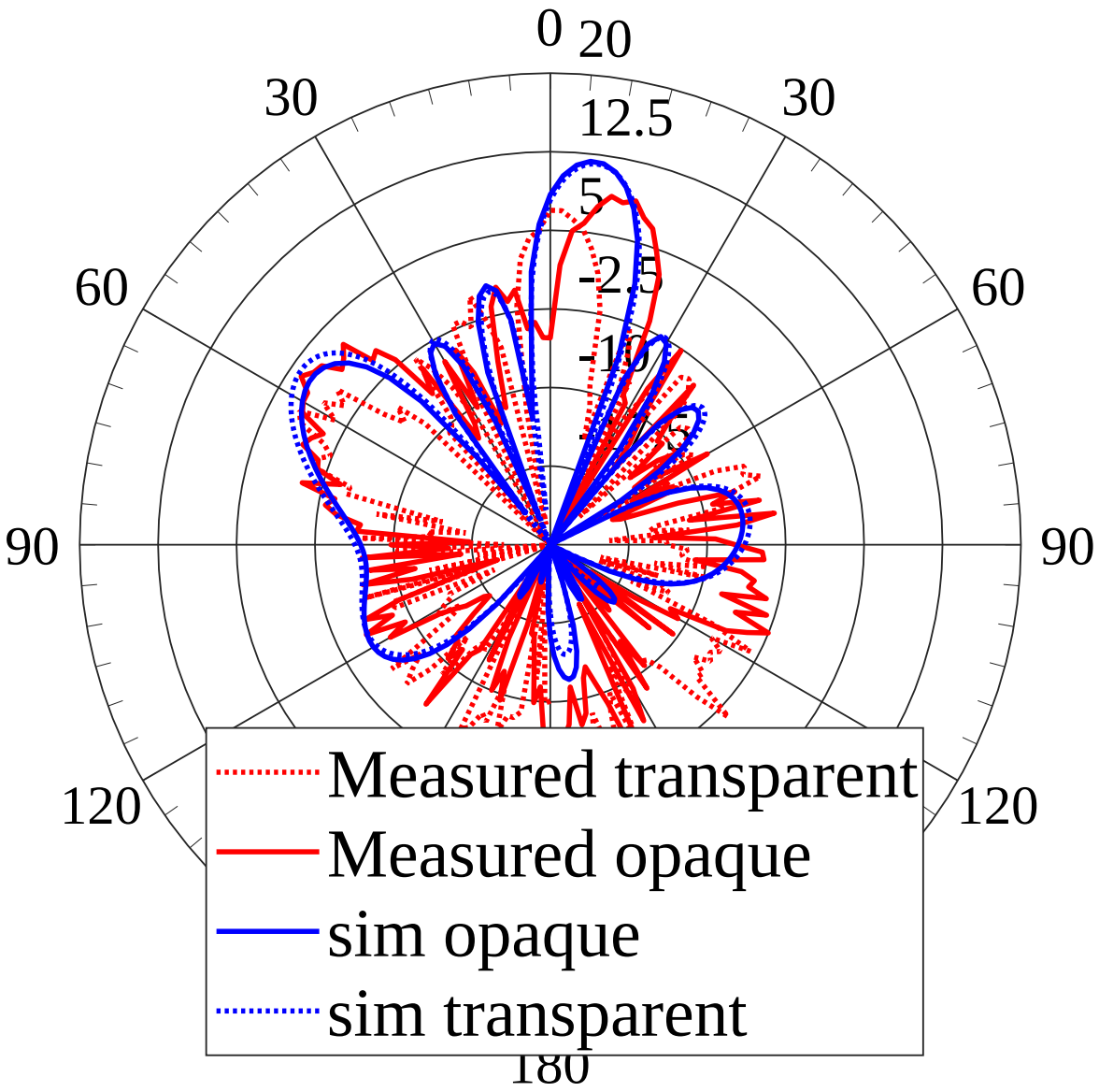

Figure 5.7: Vertically-polarized array with binary input 10, resulting in a 7^o steering angle.

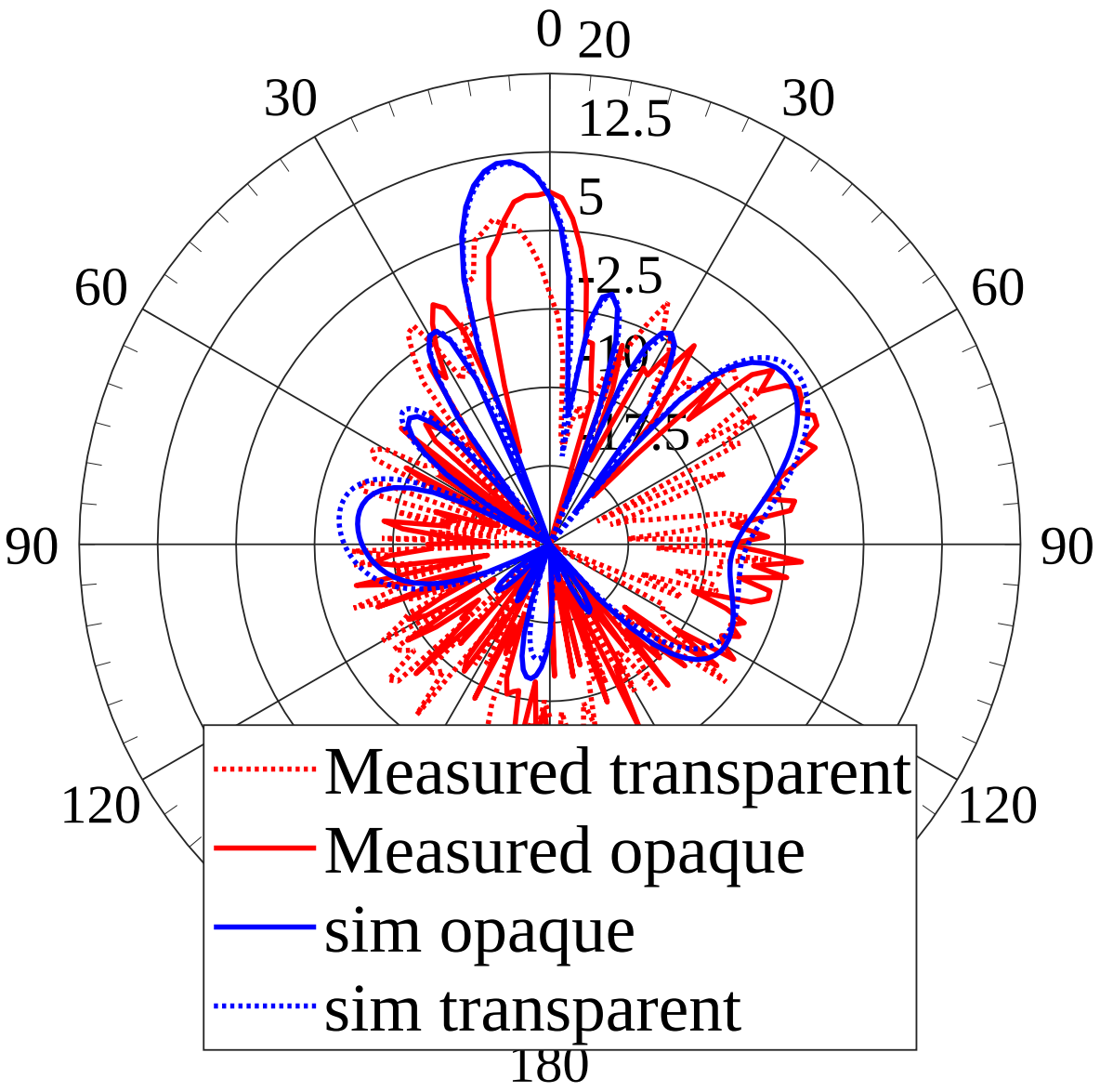

Figure 5.8: Vertically-polarized array with binary input 01, resulting in a -7^o steering angle.

5.4 Horizontally-Polarized Array

Table 5.3 shows the resulting values from the HFSS simulations and the physical experiments performed on the horizontally-polarized array. The physical experiments were performed in an anechoic chamber through the use of DAMS. The data shows that the simulated transparent array and the simulated opaque array operated similarly. It is important to note that these simulations were made using design-specified phase excitations for each of the array elements, which are presented in Table 3.1.

The measured transparent and opaque arrays operate very similarly. At the 7^o and -7^o steering angles, the horizontally-polarized transparent array has a gain roughly 3 dB lower than the opaque array. At the 22^o and -22^o steering angles, the vertically-polarized transparent array has a gain roughly 3 dB lower than the opaque array.

Figures 5.10-5.12 show azimuthal plane radiation plots comparing the performance of the simulated and measured transparent and opaque horizontally-polarized patch antennas. The azimuthal plane radiation plots of binary inputs 00 and 11, fig. 5.10 and fig. 5.9 respectively, are very similar due to the physical symmetry of the arrays and the symmetry of the phase excitations. The same comparison can be seen between the azimuthal plane radiation plots for binary inputs 01 and 10, fig. 5.11 and fig. 5.12 respectively. The main lobe -3 dB beamwidth of all horizontally-polarized antennas, both simulated and measured, are alike, producing beamwidths of 6^o to 14^o. The measured steering angle of each plot was defined as the center of each main lobe. The tolerance range is defined as the -3 dB beamwidth of the main lobe. Both the measured and simulated steering angles, similar to each other, fall within this range, proving that the antenna is successfully steered to that angle.

Table 5.3: Horizontally-Polarized Patch Antennas

Binary Input	Antenna	Max Gain (dBi)	Steering Angle (Degrees)	Beamwidth (Degrees)
00	Simulated Transparent	10.4	21^o	14^o
00	Simulated Opaque	10.4	21.5^o	13^o
00	Measured Transparent	7.2	23^o	10^o
00	Measured Opaque	8.4	29^o	10^o
01	Simulated Transparent	11.8	-7^o	14^o
01	Simulated Opaque	11.6	-6.5^o	13^o
01	Measured Transparent	5.3	-6^o	10^o
01	Measured Opaque	8.1	-1.5^o	11^o
10	Simulated Transparent	11.8	7^o	14^o
10	Simulated Opaque	11.6	7.5^o	13^o
10	Measured Transparent	5.2	12^o	10^o
10	Measured Opaque	8.8	11.5^o	13^o
11	Simulated Transparent	10.4	-21^o	14^o
11	Simulated Opaque	10.5	-21^o	14^o
11	Measured Transparent	4.4	-21^o	6^o
11	Measured Opaque	7.6	-18^o	12^o

Figure B.2 is a picture of the transparent horizontally-polarized array installed on an office window. Similar to the transparent vertically-polarized array, the transparent horizontally-polarized array successfully satisfies the transparency specification

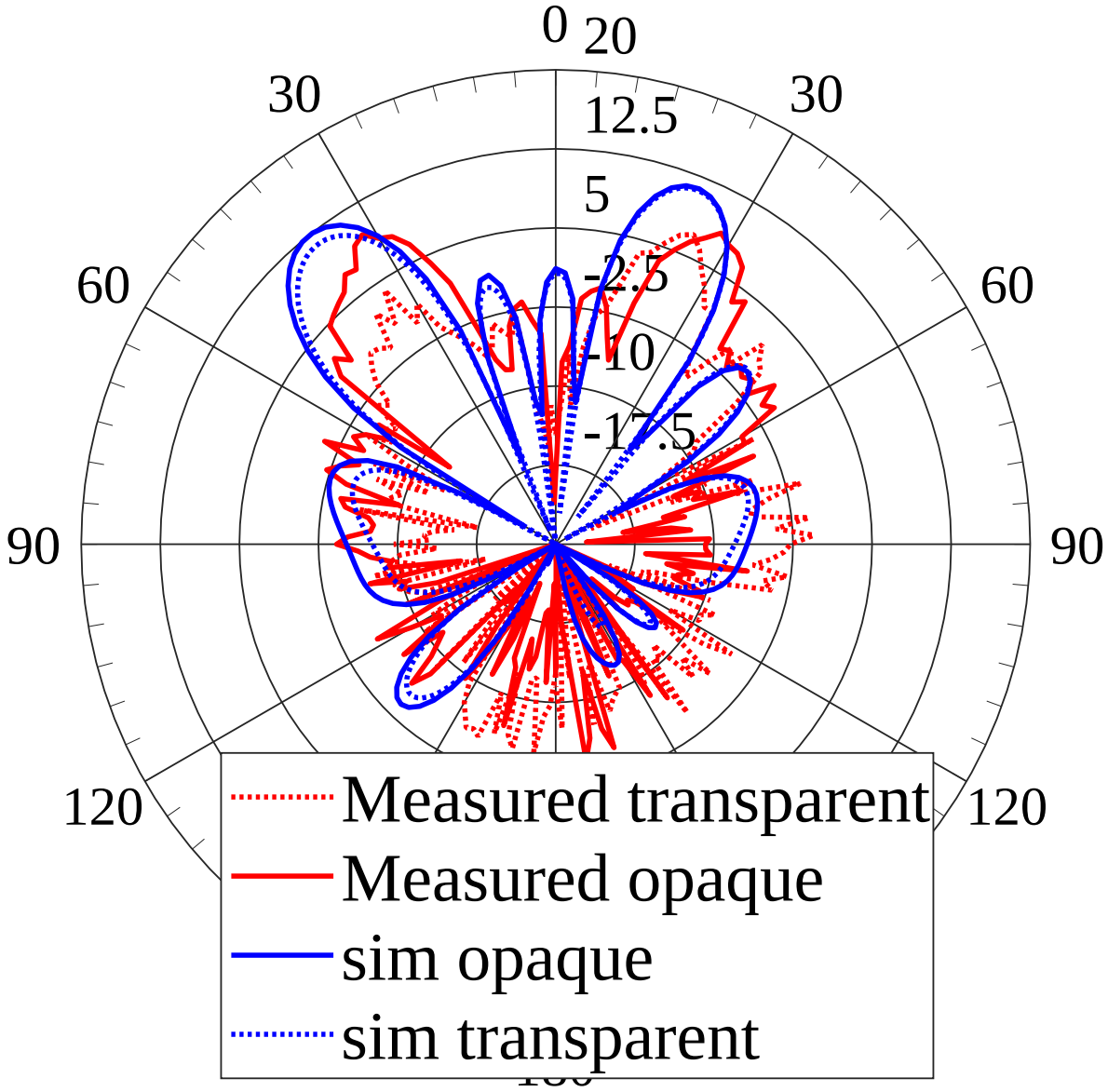

Figure 5.9: Horizontally-polarized array with binary input 00, resulting in a 22^o steering angle.

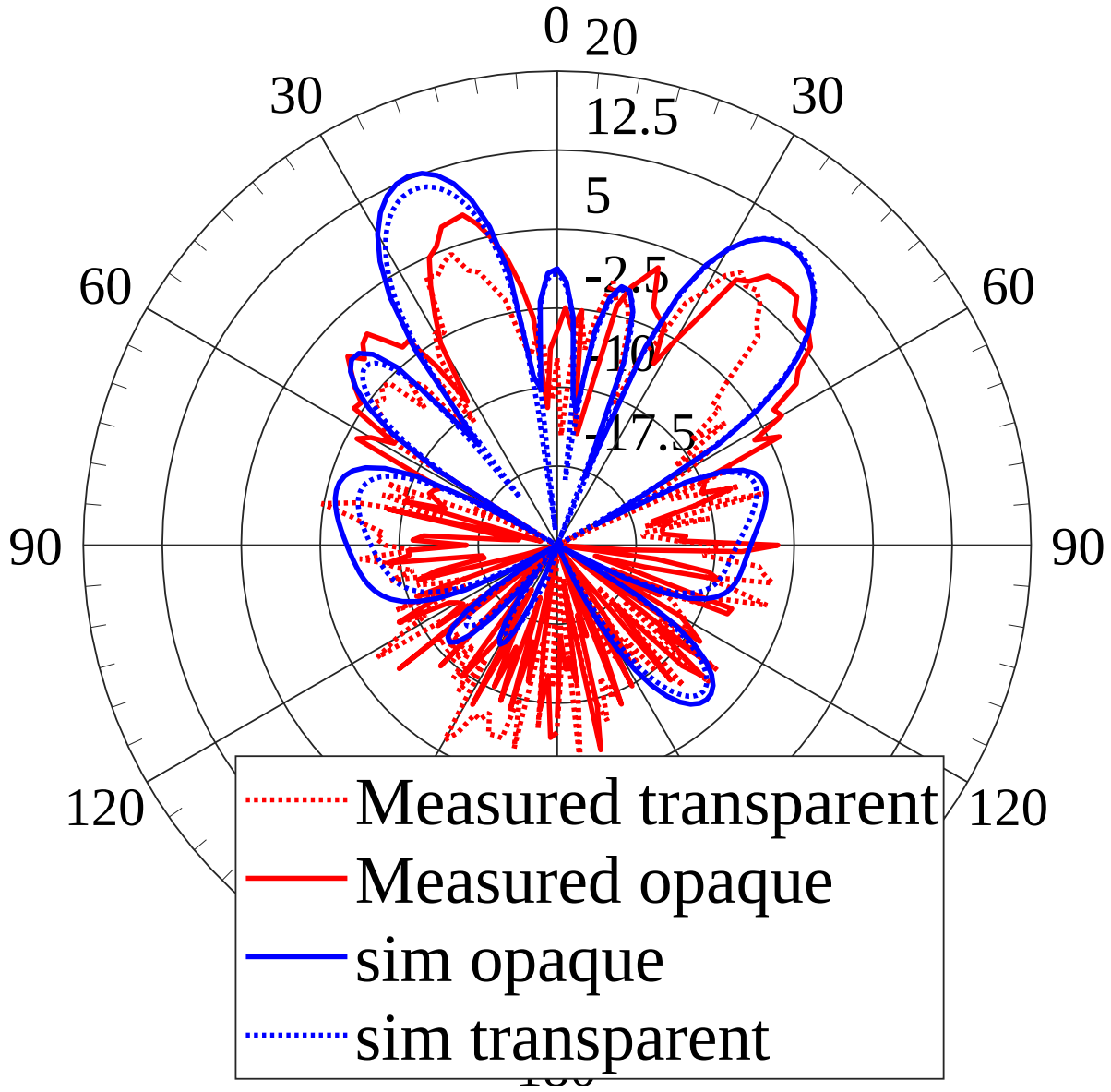

Figure 5.10: Horizontally-polarized array with binary input 11, resulting in a -22^o steering angle.

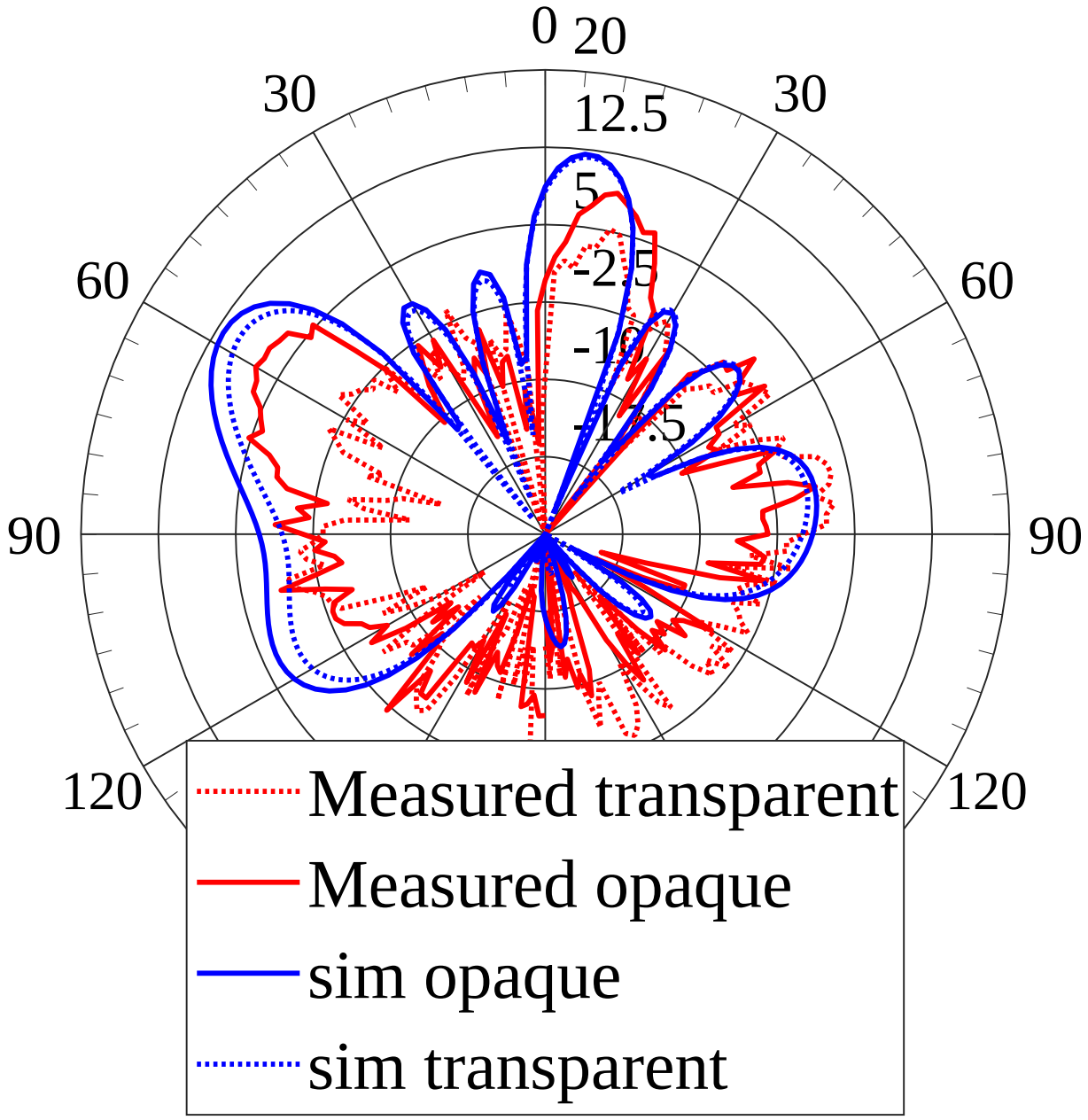

Figure 5.11: Horizontally-polarized array with binary input 10, resulting in a 7^o steering angle.

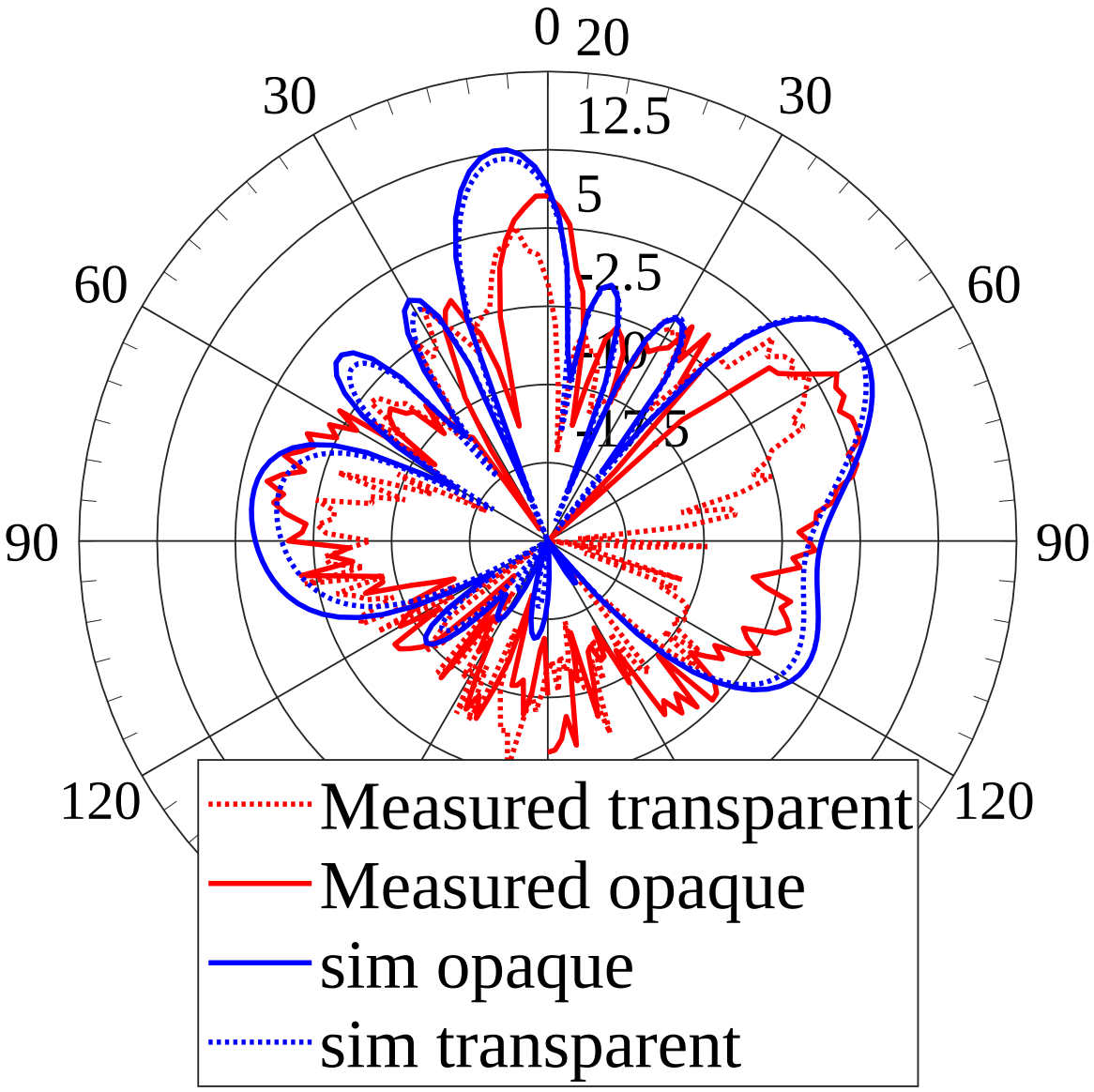

Figure 5.12: Horizontally-polarized array with binary input 01, resulting in a -7^o steering angle.

5.5 Analysis of Results

The results presented in this chapter are in line with the expected results. The two bit controller and the Butler matrix are not new technologies, meaning these components were expected to have good performance. The measurements taken from these components met expectations.

The individual transparent antenna elements were expected to perform slightly worse than the individual opaque antenna elements because of previously conducted research by Escobar *et al.* [**?**] [6]. Escobar's research showed that the transparent antenna element had a maximum gain roughly 2 dBi lower than the opaque element. The research presented in this thesis project confirms similar results. The frequency shift present in the fabricated transparent elements was unexpected. While the cause of this can't be known for certain without further investigation, it is likely related to the geometry of the mesh material used.

The spacing of the elements within each array resulted in no evidence of mutual coupling. This was expected because simulations were conducted to reduce mutual coupling intensity within the arrays.

All transparent and opaque arrays supported the four desired steering angles as expected. The gain of the transparent arrays was expected to be slightly less than that of the opaque arrays because of the performance of the transparent and opaque individual antenna elements. Overall, the transparent hardware satisfied the design goals.

The transparent vertically and horizontally-polarized patch antenna arrays presented in this research are a viable substitution for their opaque counterparts operating in the 5.5 GHz frequency band. These transparent antenna arrays will contribute to the expansion of the wireless communications infrastructure as they provide unobtrusive antenna options for a wider range of deployment environments.

CHAPTER 6

Conclusion

This thesis project aimed to develop a controllable directional transparent antenna that is easily deployed in order to facilitate the spread of high speed internet. To fulfill this goal, a vertically-polarized transparent antenna and a horizontally-polarized transparent antenna were designed, fabricated, and tested for performance. Equivalent opaque antennas were built in order to compare the performance of each of the transparent antennas to a quantifiable standard. Additionally, feed networks were built in support of beamsteering antenna functions.

The feed network was built to support four antenna functions, pertaining to four different antenna steering angles. These angles were 22^o, 7^o, -7^o, and -22^o from boresight. A Butler matrix was excited through the use of a two bit control unit in order to select a single function. The Butler matrix fed the elements within an antenna array with different phases, which provided the four different steering angles. It was important to verify the performance of this feed network before testing the antennas because it was used to excite the antennas under test. It was verified that the feed network performed properly and could support the four desired antenna functions.

The presentation of a vertically-polarized transparent antenna and the horizontally-polarized transparent antenna is the contribution to the wireless communications infrastructure. Designs of both opaque and transparent antennas were derived and simulated for analysis. Simulation results provided evidence that the opaque and transparent vertically-polarized

antennas performed alike. Simulation results showed that both the opaque and transparent horizontally-polarized antennas performed alike. Each antenna design was fabricated and tested in an anechoic chamber for performance. The anechoic chamber measurements were compared to simulation data for validation.

The performance of the opaque and transparent vertically-polarized antennas were validated by comparing simulations and measured data. The opaque and transparent vertically-polarized antennas supported the four desired steering angles. The performance of the opaque and transparent horizontally-polarized antennas were validated by comparing simulations and measured data. The opaque and transparent horizontally-polarized antennas supported the four desired steering angles. The contribution of this work is the development of a vertically-polarized transparent antenna and a horizontally-polarized transparent antenna that can be easily deployed in order to support beamsteering applications in environments where obtrusive hardware is unacceptable.

CHAPTER 7

Future Work

The goal of this research is to provide a less obtrusive option for wireless antennas hardware. One method for decreasing the optical obtrusiveness of hardware is to make the hardware transparent. This method was pursued in this thesis project and proved to be a viable solution. Another solution to this problem would be to reduce the size of the hardware. To implement this, the individual elements within the antenna array would have to be moved closer to each other, which would increase the mutual coupling between the elements and affect performance. For this to be a realistic approach, the mutual coupling between each of the elements within the array must be reduced. This can be achieved through the use of structures called metamaterials. Transparent metamaterial structures using conductive mesh technology has not yet been developed. Therefore, the future work on this project would aim to design a transparent metamaterial structure to reduce mutual coupling within the antenna array. This chapter provides brief background information on metamaterial structures, and insight as to how they can be used to further this research.

7.1 Metamaterial

Metamaterial can be used to enhance an antenna's capabilities in bandwidth, directivity, and reduce mutual coupling [50]. Metamaterial, also known as Left Handed Materials (LHM), are materials engineered to have properties that have not yet been found in nature. They are made from assemblies of multiple elements fashioned from conventional materials, such as metals or plastics. These individual elements have properties that resonate at specific

frequencies. At these specific frequencies, the elements have a negative index of refraction, or negative permittivity and permeability [51]. Using LHM changes the function of an antenna by introducing interactive electromagnetic properties.

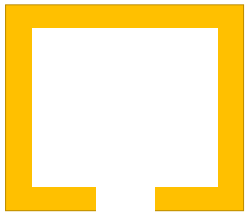

Figure 7.1: Showing a Split Ring Resonator unit cell.

A simple example of a metamaterial structure can be observed in fig. 7.1 within a unit cell of a Split Ring Resonator (SRR). The SRR structure has capacitance, inductance, and resistance. Based on these properties within the SRR structure, at specific frequencies, the structure can be modeled schematically using inductors, capacitors, and resistors.

HFSS can be utilized in order to analyze the parameters of a metamaterial unit cell. A rectangular waveguide could be modeled in order to simulate the performance of a metamaterial unit cell. Waveguides are essentially transmission lines, so by placing a unit cell inside the waveguide, the transmission line impedance changes. The impedance parameters would then be extracted from the model and exported to MATLAB, code used for the unit cell analysis is shown in Appendix C, in order to extract the constitutive parameter values of the unit cell. This information would provide an understanding on how the unit cell interacts with incident electromagnetic waves.

There are complex metamaterial structures that exist. Different structures have different constitutive parameter values. By developing a structure that can reduce mutual coupling, antenna arrays can reduce in size without negatively altering performance. This development will result in the creation of highly efficient and minimally obtrusive antennas.

Bibliography

[1] Lisa Parks. An antenna tree. *FlowJournal.org*, 2010.

[2] Eric Escobar. *A Coplanar Edge-Fed Optically-Transparent Microstrip Patch Antenna Operating in the 5-6 GHz Frequency Spectrum.* Masters Thesis, University of New Hampshire, Durham, New Hampshire, 2015.

[3] Brian Regal. *Radio: The Life Story of a Technology.* Greeenwood Technographies. Greenwood, 2005.

[4] John W. Klooster. *Icons of Invention: The Makers of the Modern World from Gutenberg to Gates*, volume 1. ABC-CLIO, 2009.

[5] K. Siwiak. *Radiowave Propagation and Antenna for Personal Communications.* Artech House, Inc, 2nd edition, 1998.

[6] Eric Escobar, Nick Kirsch, George Kontopidis, and Brough Turner. A 5.5 GHz Optically Transparent Mesh Wire Microstrip Patch Antenna. *Electromagnetic Research Symposium in Stockholm, Sweden*, 2013.

[7] Tursunjan Yasin, Reyhan Baktur, and Cynthia Furse. *A comparative study on two types of transparent patch antennas.* IEEE, August 2011.

[8] Peter Halevi. *Spatial Dispersion in Solids and Plasmas.* Amsterdam: North-Holland, 1992.

[9] Clifford Truesdell and Walter Noll. *The Non-linear Field Theories of Mechanics.* Springer, 2004.

[10] Mailadil T. Sebastian. *Dielectric Materials for Wireless Communications.* Elsevier, 2008.

[11] Peter Y. Yu and Manuel Cardona. *Fundamentals of Semiconductors: Physics and Materials Properties.* Berlin: Springer, 2001.

[12] Hartmut Haug and Stephan W. Koch. *Quantum Theory of the Optical and Electronic Properties of Semiconductors.* World Scientific, 1994.

[13] John David Jackson. *Classical Electrodynamics.* New York: John Wiley and Sons (WIE), 2nd edition, 1975.

[14] Ralph P. Winch. *Electricity and Magnetism.* Prentice Hall, 1955.

[15] Eric Bogatin. *Signal Integrity: Simplified*. Prentice Hall Professional, 2004.

[16] P. R. Gray, R. G. Meyer, P. J. Hurst, and S. H. Lewis. *Analysis and Design of Analog Integrated Circuits*. New York: John Wiley and Sons (WIE), 4th edition, 2001.

[17] R. C. Jaeger and T. N. Blalock. *Microelectronic Circuit Design*. United States: McGraw-Hill Higher Education, 2008.

[18] R. Ludwig and G. Bogdanov. *RF Circuit Design: Theory and Application*. Prentice Hall, 2nd edition, 2008.

[19] E. Bogatin. *Signal and Power Integrity: Simplified*. United States: Prentice Hall Professional Technical Reference, 2009.

[20] D. J. Griffiths. *Introduction to Quantum Mechanics*. United Kingdom: Pearson Prentice Hall, 2nd edition, 2004.

[21] S. Ramo, J. R. Whinnery, and T. Van Duzer. *Fields and Waves in Communication Electronics*. United States: John Wiley and Sons (WIE), 33rd edition, 1994.

[22] D. M. Pozar. *Microwave Engineering*. United States: John Wiley and Sons (WIE), 3rd edition, 2004.

[23] G. L. Matthaei, L. Young, and E. M. T. Jones. *Microwave Filters, Impedance-Matching Networks and Coupling Structures*. United States: Artech House Publishers, 1980.

[24] Christophe Caloz and Tatsuo Itoh. *Electromagnetic Metamaterials: Transmission Line Theory and Microwave Applications*. Wiley, John & Sons, Incorporated, 2005.

[25] K. B. Wolf. Geometry and Dynamics in Refracting Systems. *European Journal of Physics*, 16, 1995.

[26] John D. Joannopoulos, S. G. Johnson, J.N. Winn, and R.D. Meade. *Photonic Crystals: Molding the Flow of Light*. Princton NJ: Princeton University Press., 2nd edition, 2008.

[27] D. G. Fink and D. Christiansen. *Electronics Engineers' Handbook*. New York: McGraw-Hill Publishing Co., 3rd edition, 1988.

[28] J. Ryder. *Networks, Lines and Fields*. New York: Prentice-Hall Electrical Engineering Series, 1949.

[29] David S. Hecht, Liangbing Hu, and Glen Irvin. Emerging Transparent Electrodes Based on Thin Films of Carbon Nanotubes, Graphene and Metallic Nanostructures. *Wiley-VCH Verlag GmbH & Co.*, 23(13), 2011.

[30] T. Kawashima, H. Matsui, and N. Tanabe. New transparent conductive films: FTO coated ITO. *Thin Solid Films*, 445(2), 2003.

[31] S. H. Wei, X. Nie, and S. Zhang. Electronic structure and doping of p-type transparent conducting oxides. *Photovoltaic Specialists Conference, Conference Record of the Twenty-Ninth IEEE*, May 2002.

[32] J. Saberin and C. Furse. Challenges with optically transparent patch antennas. *IEEE*, 54(3), August 2012.

[33] H. J. Song, T. Y. Hsu, D. Sievenpiper, H. P. Hsu, J. Schaffner, and E. Yasan. A method for improving the efficiency of transparent film antennas. *IEEE*, 7, October 2008.

[34] N. Guan, H. Furuya, K. Himeno, K. Goto, and K. Ito. A monopole antenna made of a transparent conductive film. *Antenna Technology: Small and Smart Antennas Metamaterials and Applications, 2007. IWAT '07. International Workshop*, March 2007.

[35] U. Avachat, F. Yan, D. Metacarpa, and P. Haldar. Impacts of humidity and temperature on the performance of transparent conducting indium tin oxide and electrical interconnects for solar applications. *Photovoltaic Specialists Conference (PVSC) 2013 IEEE*, June 2013.

[36] Terje A. Skotheim and John Reynold. *Handbook of Conducting Polymers*. CRC Press, 1998.

[37] B. Pregan and M. Gratzel. *A low-cost, high-efficiency solar cell based on dye-sensitized colloidal Ti02 films*. Nature, 1991.

[38] N. Kirsch, N. Vacirca, T. Kurzweg, A. K. Fontecchio, and K. Dandekar. Performance of transparent conductive polymer antennas in a MIMO ad-hoc network. *Wireless and Mobile Computing, Networking and Communications (WiMob), 2010 IEEE 6th International Conference*, 2010.

[39] J. Nevrela, M. Micjan, M. Novota, S. Flickyngerova, J. Kovac, M. Pavuk, P. Juhasz, J. Jakabovic, and M. Weis. Technology of conductive polymer PEDOT:PSS films. *Advanced Semiconductor Devices Microsystems (ASDAM)*, October 2014.

[40] T. W. Turpin and R. Baktur. See-through microstrip antennas and their optimization. *Gen. Assemb. Int. Union Radio Sci.*, 2008.

[41] J. Hautcoeur, F. Colombel, X. Castel, M. Himdi, and E. M. Cruz. Radio frequency performances of transparent ultra-wideband antennas. *Progress in Electromagnetics Research*, 22, 2011.

[42] Constantine A. Balanis. *Antenna Theory Analysis and Design*. John Wiley and Sons Inc, 3rd edition, 2005.

[43] M. E. Van Valkenburg. *Network Analysis*. Prentice Hall College Div, 3rd edition, 1974.

[44] Constantine A. Balanis. *Theory, Analysis, and Design*. John Wiley and Sons Inc, 2nd edition, 1982.

[45] David K. Cheng. *Field and Wave Electromagnetics*. Addison-Wesley Publishing Company Inc., 2nd edition, 1998.

[46] W. L. Stutzman and G. A. Thiele. *Antenna Theory and Design*. New York: Wiley, 3rd edition, 2013.

[47] A. I. Zverev. *Handbook of Filter Synthesis*. Wiley New York, 1967.

[48] James H. Harlow. *Electric power transformer engineering*. CRC Press, 2004.

[49] Michael H. Tooley. *Electronic Circuits: Fundamentals and Applications*. Routledge, 3rd edition, 2006.

[50] Nathan Landy, John Hunt, and David R. Smith. Homogenization Analysis of Complementary Waveguide Metamaterials. *Photonics and Nanostructures - Fundamentals and Applications*, 11(4), November 2013.

[51] M. Anand. Applications of Metamaterial in Antenna Engineering. *International Journal of Technical Research and Applications*, 2014.

Appendix A. **Fabrication**

A.0.1 Materials Used During Transparent Hardware Fabrication

This section explains the items and materials used in the fabrication of the transparent antennas. In order to efficiently reproduce this work, it is important that each mentioned material is present during the fabrication process.

The first item is rubbing alcohol, fig. A.1. Rubbing alcohol was used to clean Lexan surfaces, easily removing excess glues, epoxies, and related debris. The type of cloth used with rubbing alcohol was important because cloths made with loose fibers are susceptible to shedding when they are wiped on surfaces. Clean room grade microfiber cloths were used for this reason, fig. A.2. Furthermore, clean room grade cue tips were used. These cue tips are capable of removing precise amounts of debris from the workspace. Lastly, tape was used in order to protect surfaces from liquids and glues. Tape greatly reduced the intensity of problems given a spill or over application of glue or epoxy.

Figure A.1: Rubbing Alcohol.

Figure A.2: Clean room grade microfiber cloths.

Lexan, made by Bayer, was used as the dielectric material in this thesis project because of its dielectric properties, cost, and transparency. A very large sheet of Lexan was purchased so that all transparent hardware was fabricated from a single board. This mitigated differences between Lexan used in any hardware.

Wearing latex gloves throughout the fabrication process was important for the aesthetic quality of the physical model. The aesthetics of the physical model are damaged by finger prints and debris, forever encapsulated between transparent layers of the hardware. Furthermore, the transparent mesh material is very brittle, so mishandling it in any way could break micro-thin wires, creating electrical discontinuity within the physical model.

The glue used to bond the conductive mesh material to Lexan was Bondic. Bondic is a commercially purchased glue that cures with ultraviolet light exposure. As seen in fig. A.3, the Bondic kit came with an ultraviolet light and a couple tubes filled with the Bondic glue. The glue was easy to squeeze from the black tubes and was also easy to clean up if a mistake was made. The glue cured and hardened after approximately five seconds of ultraviolet light exposure. The cured Bondic was similar to a transparent plastic. This made gluing the conductive mesh material to Lexan very easy.

Figure A.3: The transparent ultraviolet curing glue, Bondic.

Lastly, the material used to electrically connect the transparent mesh material to the edge board was a silver epoxy. Figure A.4 shows the packaging of the silver epoxy used. This silver epoxy came in two tubes. In a side dish, the contents of the two tubes were mixed in equal parts and then applied to the desired areas of the physical model. This epoxy worked well because the epoxy did not harden immediately, giving an adequate amount of time to properly place components.

Figure A.4: Silver epoxy used to create electrical continuity between mesh material and edge board.

A.0.2 Fabricating the Transparent Antennas

This section explains the physical steps taken to fabricate the transparent antennas. The fabrication process for the vertically-polarized transparent antenna and the horizontally-polarized transparent antenna are identical. Pictures shown in this section may show a vertically-polarized component and then a horizontally-polarized component in the next step. This was done because the clearest pictures were selected in order to best represent each step of the process.

The first step in fabrication was milling the Lexan board. This was done so that the edge board could fit flush into the Lexan. It was very important that the edge board surface was exactly on the same plane as the Lexan surface because the antenna elements that attached to the edge board are required to be parallel to the ground plane. If a bend were present, the microstrip transmission line would interact with the ground plane differently than intended. A high precision milling machine, made by Bridgeport, was used to satisfy these requirements. Figure A.5 shows the Lexan placed on the milling machine's work space and fig. A.6 shows the Lexan after the first cut was made. The latter picture also shows a piece of wood clamped on top of the Lexan. This wood was used to dampen the vibrations while the Lexan was being milled. The final precise cutting used a quarter inch thick sheet of aluminum placed on either side of the Lexan, forming a Lexan sandwich. The aluminum sheeting was stronger than the wood sheets and was perfect to eliminate the Lexan vibrations.

Figure A.5: Lexan board sitting in milling workspace.

Figure A.6: Lexan board cut on milling machine.

The finished product from the milling machine step is shown in fig. A.7. As seen in this figure, there was a milled area for the edge board to be mounted, there are five small holes, and four oval cuts. The five small holes line up perfectly with the five small holes in the edge board, allowing for nylon screws to help hold the edge board to the Lexan. The four oval shaped holes were how tabs on the mesh ground plane connect to the edge board ground plane.

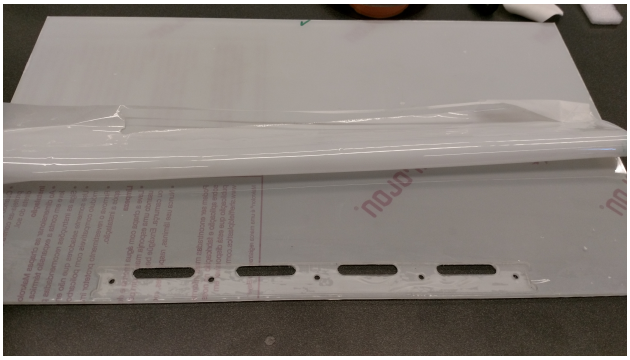

Figure A.7: Showing the cut into the Lexan made by the milling machine.

Figure A.8 shows the edge board being placed into the Lexan. Figure A.9 shows the edge board properly placed into the Lexan. The nylon screws are seen in this figure, ensuring that the edge board is properly attached to the Lexan. Although the milled cut was precisely made, there still existed a microscopic crack between the edge board and the wall of the cut Lexan. For this reason, an isolation step was added, which included applying Bondic glue within the crack. This prevented silver epoxy from oozing or spilling between the edge board and Lexan, which would have caused a short circuit between the transmission line side and the ground plane side of the edge board. This step is shown in fig. A.10.

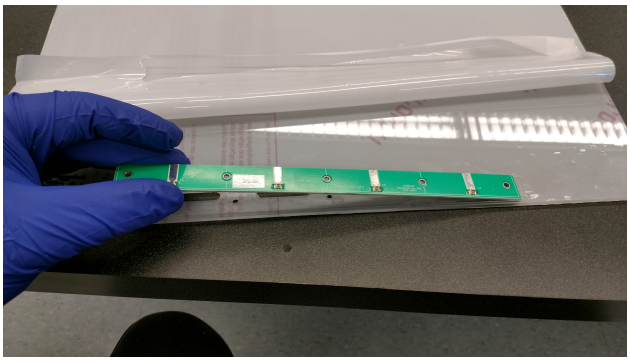

Figure A.8: Placing the edge board into the milled Lexan.

Figure A.9: Edge board placed into milled lexan.

Figure A.10: Ensuring isolation from the patch side of the antenna and the ground side of the antenna.

Cleanliness of the Lexan surface is important for many reasons. First, in order to maintain maximum transparency, debris and smudges were removed from the Lexan surface. Secondly, gluing to a clean surface, versus a dirty surface, ensures proper adhesion between materials. Lastly, the conductive mesh has very small wires. When introduced to oils or other substances, these wires will corrode. Corrosion of these wires will greatly reduce the performance of this hardware. Figure A.11 shows a microfiber cloth soaked in rubbing alcohol cleaning the Lexan surface.

Figure A.11: Cleaning the surface where the patch antennas will be attached.

Another cleaning step, both aesthetic and performance related, uses tape. Taping the surrounding area of the transmission line on the edge board allowed for easy application and clean up of silver epoxy. The application of tape is shown in fig. A.12 and is explained further in the silver epoxy application step.

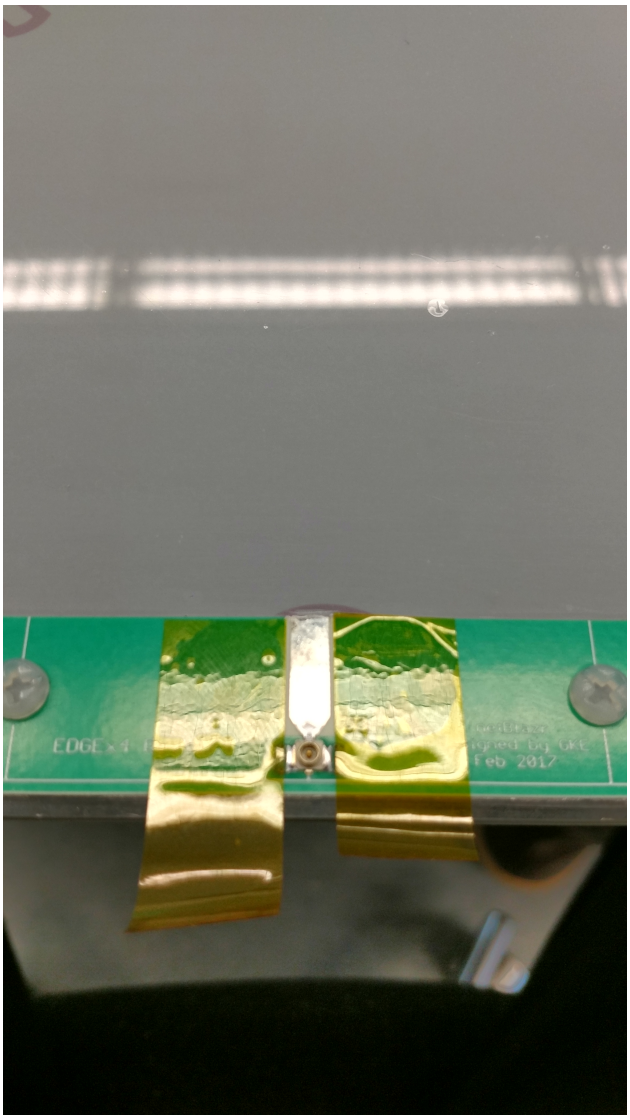

Figure A.12: Taping the transmission line side of the edge board for clean epoxy application.

After the edge board was properly installed, and the surface of Lexan was clean, it was time to glue the transparent patch antennas to the Lexan. The first step was to cover the mesh side of the transparent mesh material with Bondic glue. It is required that the side of the mesh patch antenna that has the exposed silver mesh wires is the side that was glued to the Lexan surface. This ensured that the conductive side of the mesh material was on the correct side when it came time to silver epoxy the mesh transmission line to the edge board transmission line. The transmission line portion of the mesh patch antenna was held with one hand to align with the edge board transmission line, as the other hand held the patch

antenna. Then, the hand that held the patch antenna let go of the patch antenna allowing it to fall freely onto the surface of the Lexan. Figure A.13 and A.14 show this process. This method was practiced with scrap mesh material many times and was found to be the optimal procedure to reduce air bubbles between the patch antenna and Lexan.

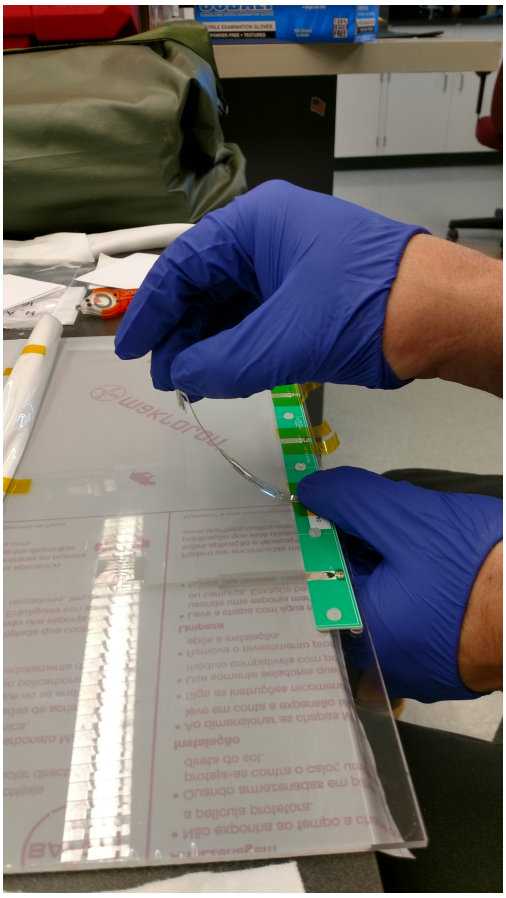

Figure A.13: Placing a glue covered patch.

Figure A.14: Alligning mesh antenna into proper position.

Pressing down on the patch antenna helped push air bubbles out from under the patch antenna. It also pushed excess glue out from under the patch antenna onto the exposed surface of the Lexan. Using ultraviolet light, Bondic was cured underneath the patch, shown in fig. A.15. It was important that when this was done none of the excess Bondic was cured. The excess uncured Bondic was then removed, shown in fig. A.16. The process of curing a small amount of Bondic underneath the patch was done so that when the excess Bondic was wiped up it didn't move the location of the patch. Once all excess Bondic was removed, the Bondic underneath the patch was completely cured to fasten the patch to the Lexan surface.

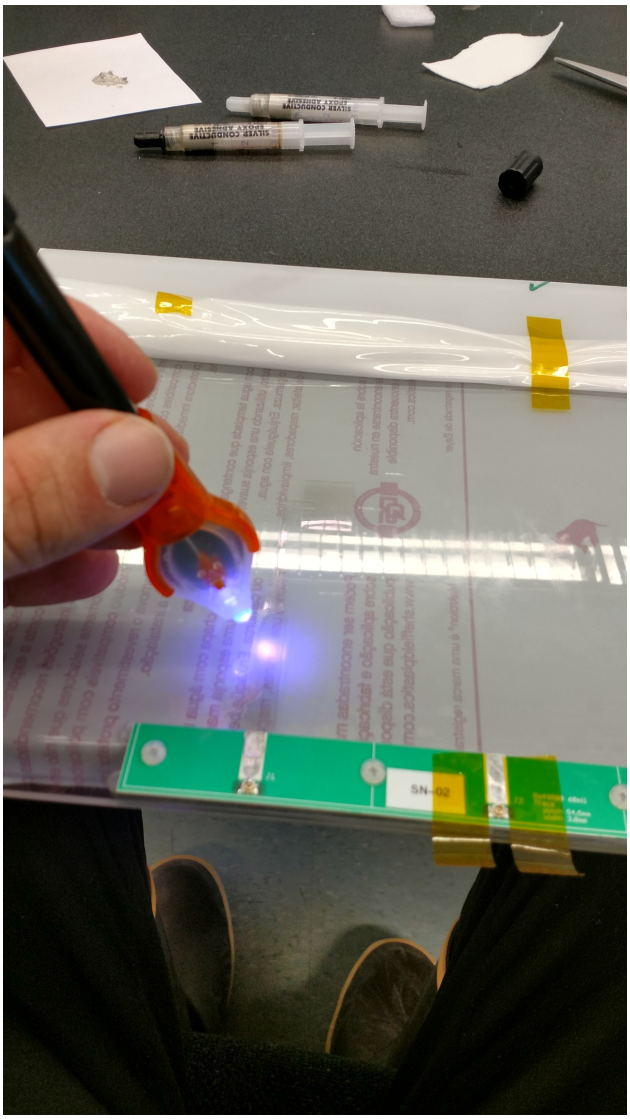

Figure A.15: Applying ultraviolet light to cure the Bondic between the Lexan and the patch antenna.

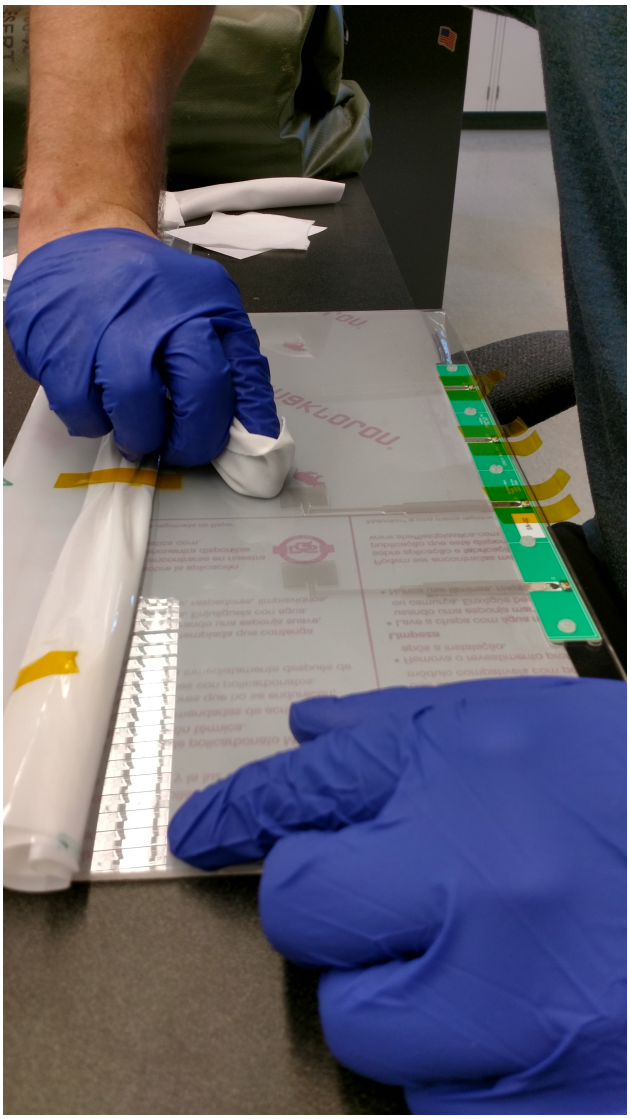

Figure A.16: Cleaning extra Bondic off of the Lexan surrounding the patch.

Now that the mesh patch antenna was glued to the Lexan surface, the next step was to electrically connect the mesh patch antenna to the edge board. A clean room grade cue tip was used to place mixed silver epoxy between the mesh patch antenna and the transmission line on the edge board. Silver epoxy was then applied, this is shown in fig. A.17. Figure A.18 shows the removal of tape beside the transmission line that was just epoxied. By removing the tape after the application of epoxy, the extra epoxy that oozed out from the connection between the mesh transmission line and the edge board's transmission line was removed. It was important to remove this silver epoxy because changes in width of the transmission line would effect performance.

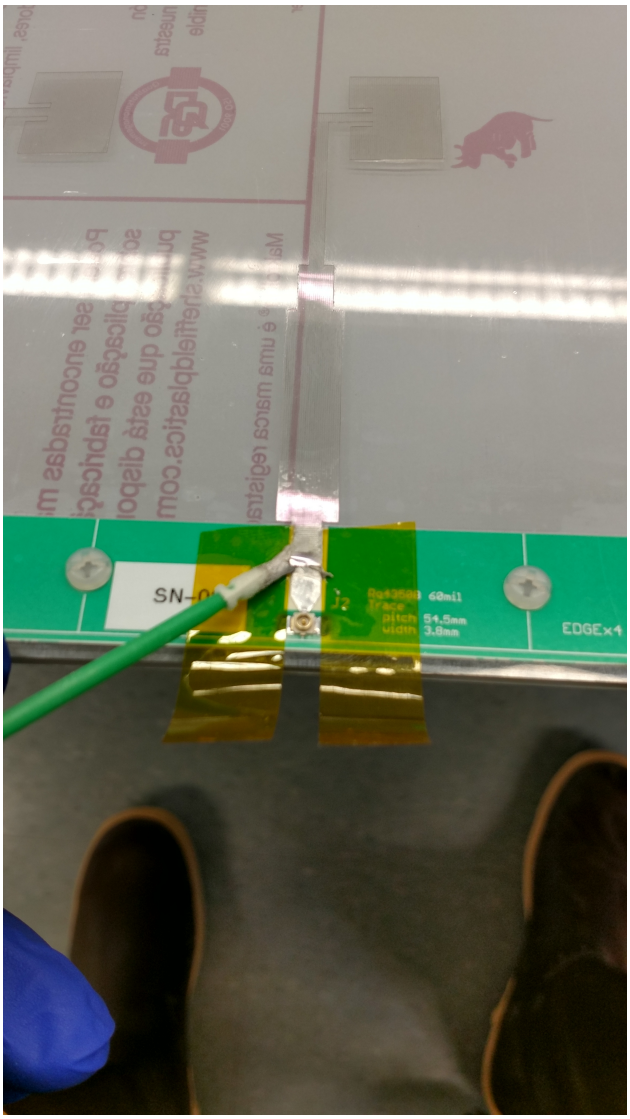

Figure A.17: Applying silver epoxy for electrical continuity.

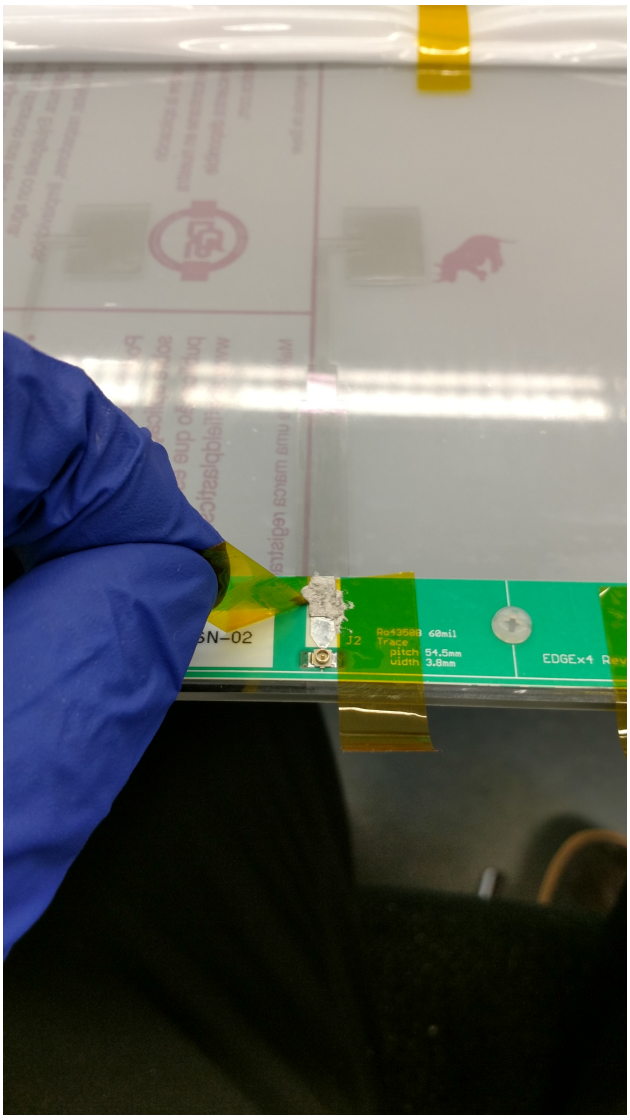

Figure A.18: Removing the tape from the edge board.

Figure A.19 shows a completely glued and epoxied mesh patch antenna onto the Lexan and edge board. Figure A.20 shows arrays mounted onto Lexan. Furthermore, it is shown that the protective sheet that originally covered the Lexan surface was rolled and taped, not simply removed. This was done so that it could be unrolled back onto the Lexan surface in order to protect the patch side of the antenna while the ground plane side was being worked attached.

Figure A.19: Top view of a single element.

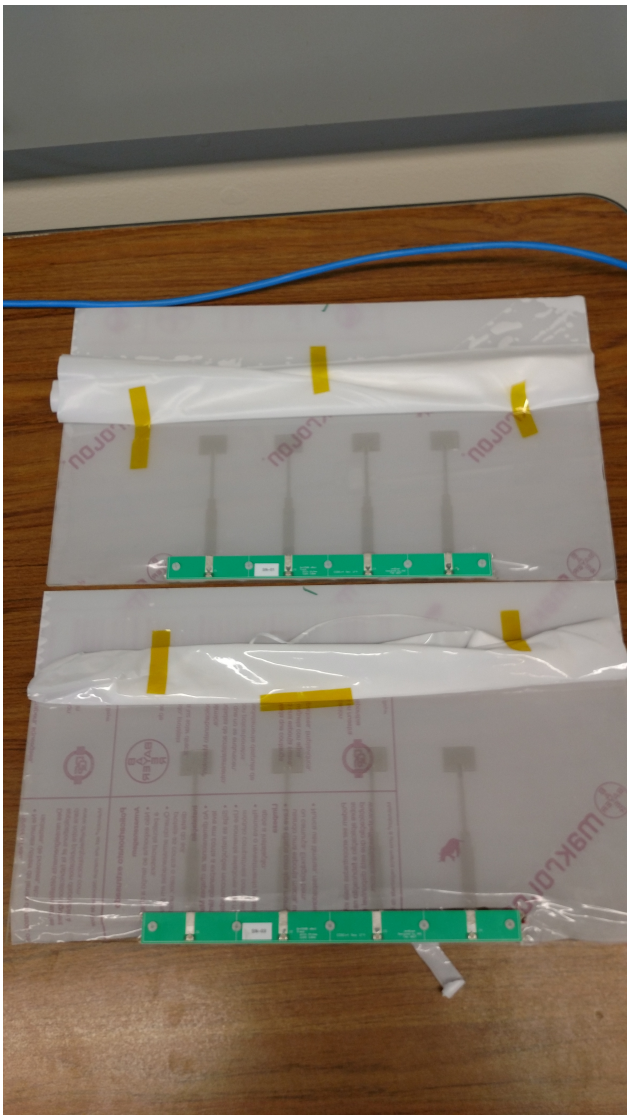

Figure A.20: The finished patch side of the antenna array.

Figure A.21 shows that a manila folder was used as a template for cutting the ground plane, ensuring that all ground planes were cut to the same size. As shown in fig. A.22, tabs are cut in the ground plane that were used to connect the mesh ground plane and the edge board ground plane.

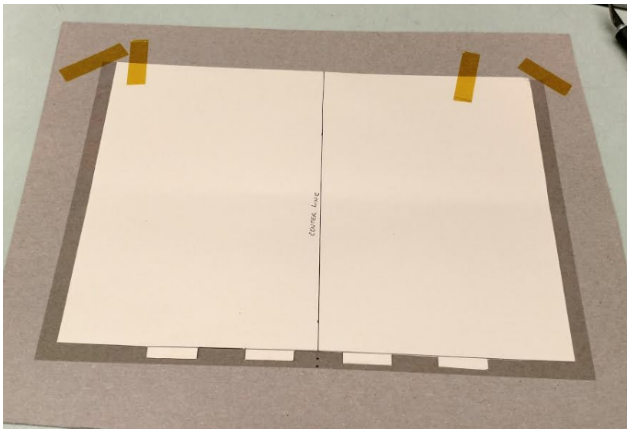

Figure A.21: Placing the template onto mesh in order to cut properly sized tabs in ground plane.

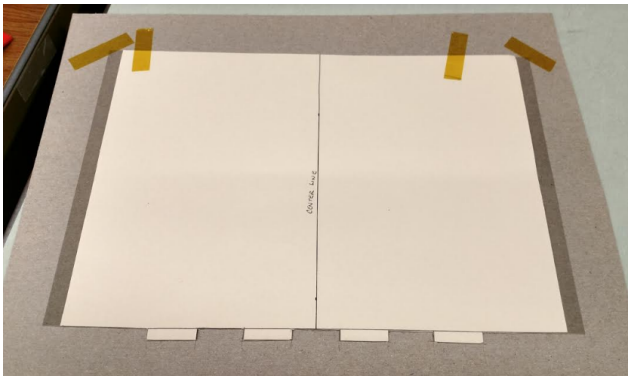

Figure A.22: Cutting the ground plane from a template.

Cleanliness is important for the ground plane side of the antenna as well. Figure A.23 shows cleaning the Lexan surface on the ground plane side of the array. Figure A.24 shows that tape was placed over the holes cut in the Lexan that expose the ground plane of the edge board. It was important to tape over these holes while applying the mesh ground plane in the event that glue was spilled. If glue was spilled into these holes, and onto the edge board ground plane, the mesh ground plane's connection to the edge board would be negatively effected.

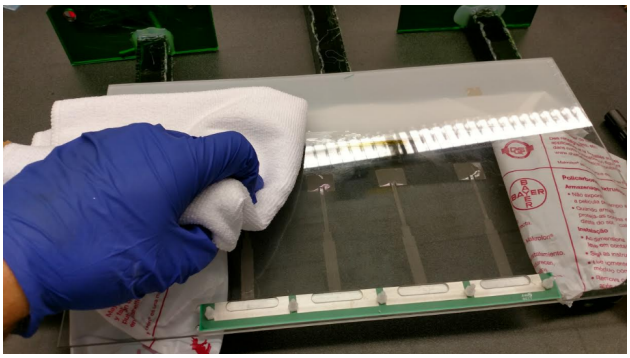

Figure A.23: Cleaning the surface where the ground plane will be attached.

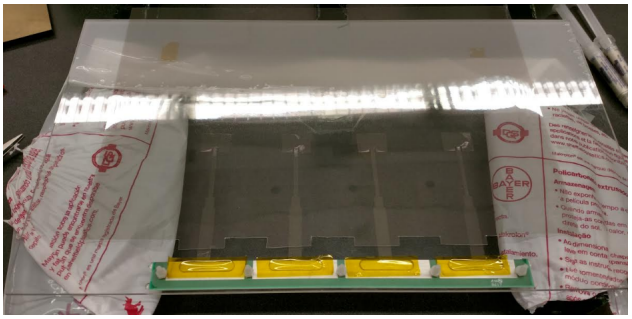

Figure A.24: Taping the ground plane of the edge board to prepare for ground plane gluing.

Figure A.25 shows how the ground plane side of the Lexan was covered in Bondic glue to connect the mesh ground plane to the Lexan. The amount required for this step needs to be optimized for manufacturing. I used three Bondic glue capsules on each antenna ground plane in this project. Figure A.26 shows how the mesh ground plane was introduced to the Bondic covered Lexan surface. This step is very messy. For this reason, it was important to keep the work space organized and clean.

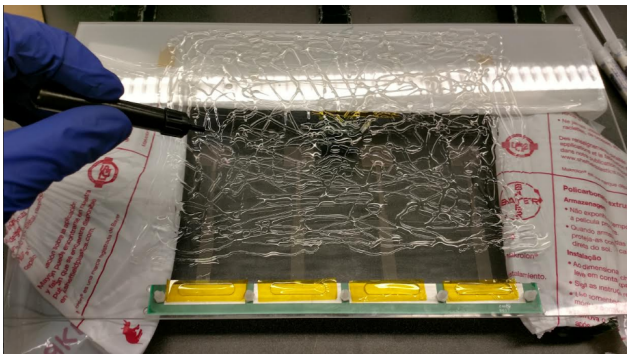

Figure A.25: Applying glue to the area that the ground plane will be attached to the Lexan.

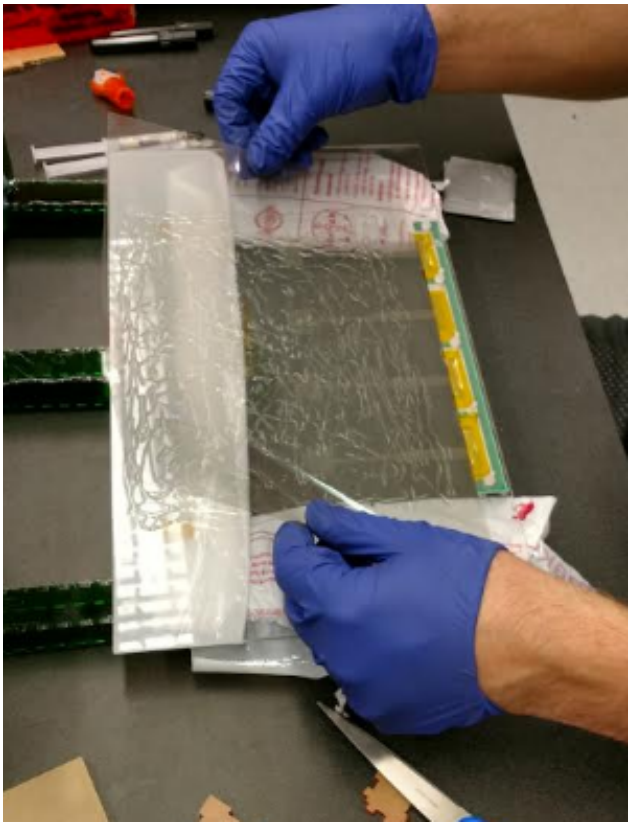

Figure A.26: Placing the ground plane onto the glue covered Lexan.

Figure A.27 depicts the step in which all the Bondic glue was smoothed out between the Lexan and the mesh ground plane. A squeegee was used to facilitate this step. This was done so that all the air bubbles were removed from between the layers, which led to the highest overall transparency. Just like the mesh patch antenna gluing procedure, once the air bubbles were removed from an area, that area was cured so that the mesh could maintain its position on the surface while further squeegeeing and cleaning were conducted. Figure A.28 shows this step.

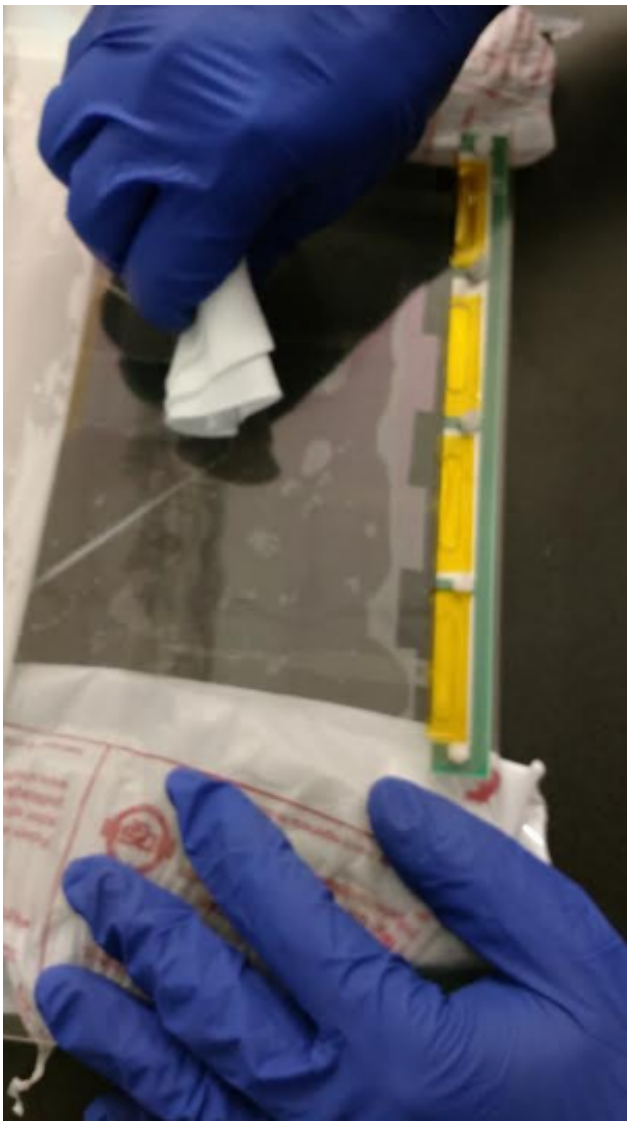

Figure A.27: Using a squeegee to push air bubbles out from between the ground plane and Lexan.

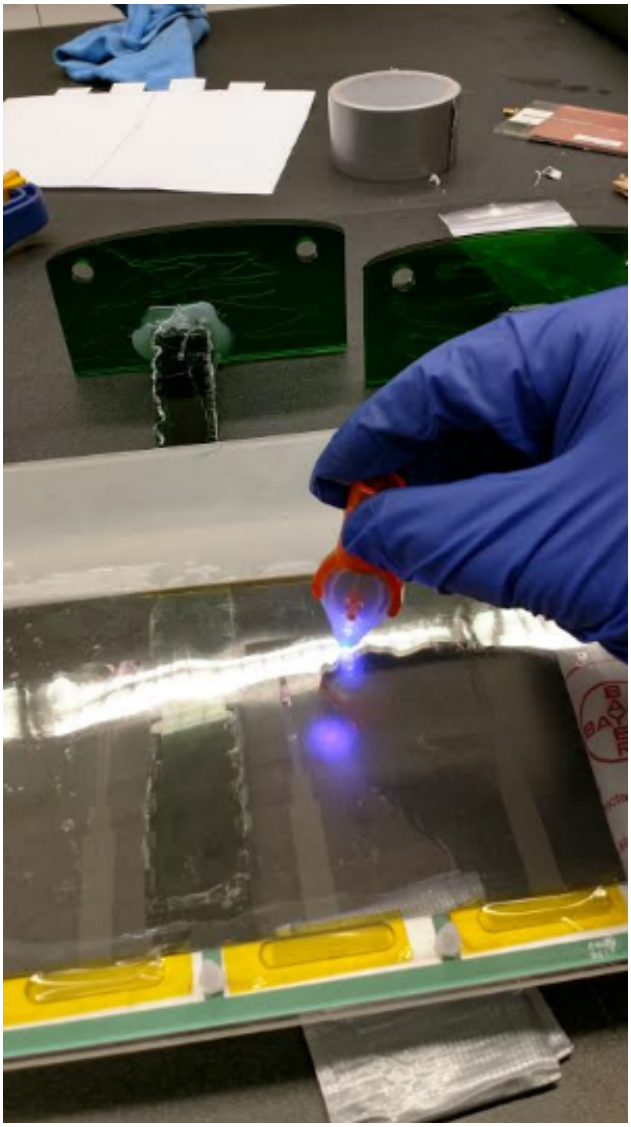

Figure A.28: Applying ultraviolet light to cure the Bondic between the Lexan and the ground plane.

Finally, the mesh ground plane was glued to the edge board ground plane. This was done by placing a significant amount of silver epoxy between the mesh ground plane tabs and the edge board ground plane, shown in fig. A.29. After this application was made, the extra silver epoxy was removed, shown in A.30. The antenna was left for approximately 12 hours in order to ensure that all epoxy was cured. The antenna fabrication is now complete.

Figure A.29: Creating electrical continuity between the edge board and the ground plane using silver epoxy.

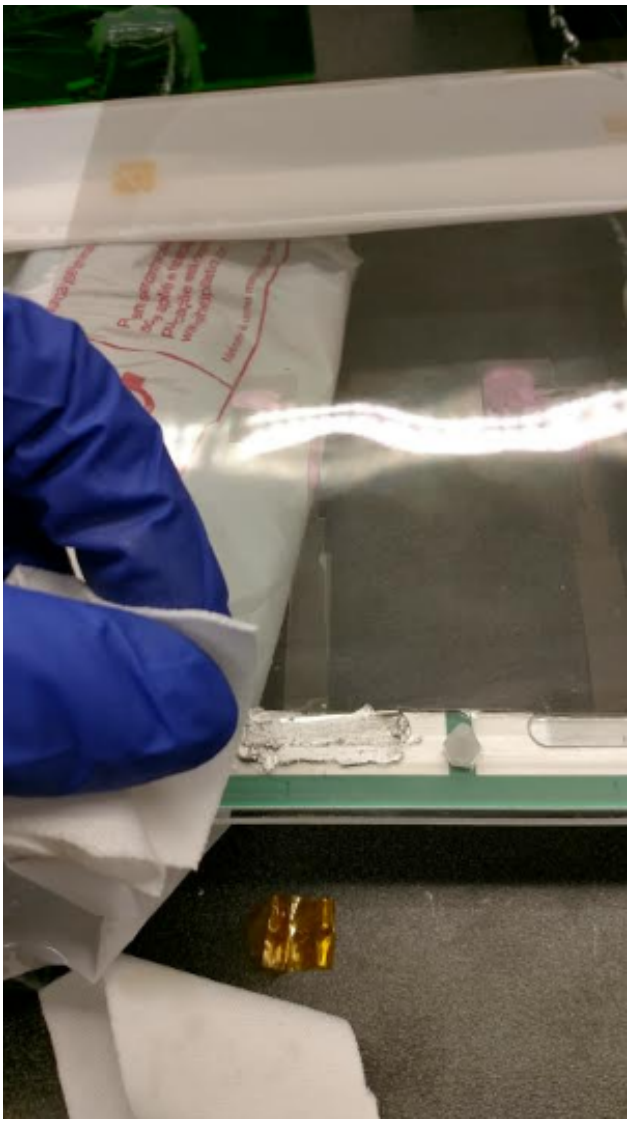

Figure A.30: Cleaning extra silver epoxy off of ground plane connection.

Appendix B. **Deployed Transparent Hardware Pictures**

Figure B.1: Deployed vertically-polarized transparent antenna array.

Figure B.2: Deployed horizontally-polarized transparent antenna array.

Appendix C. MATLAB Code For Metamaterial Analysis

clear all;
num=xlsread('meta2');
freq=num(:,1);
$C = 0.30; (Speedoflightinfreespacein10^9)$
$ax = 0.033; (sizeofthecellinm)$
$k0 = (2 * pi. * freq)./C; (wavevector)$
(Z-parameter extracted from HFSS in real and imaginary numbers)
z11re=num(:,2);
z11im=num(:,3);
z11=((z11re)+i*(z11im));
z12re=num(:,2);
z12im=num(:,5);
z12=((z12re)+i*(z12im));
z21re=num(:,6);
z21im=num(:,7);
z21=((z21re)+i*(z21im));
z22re=num(:,8);
z22im=num(:,9);
$z22 = ((z22re) + i * (z22im)); (ImpedanceDefinition)$ Zo=400;
Zline=400;
ABCD Parameters
A=(z11./z21);
$B = (((z11. * z22) - (z21).^2)./(z21));$
C=(1./z21);
D=(z22./z21);
(Extraction of parameters)
gamma=acos((A+D)./2)./d;
Zb=(B./((exp(-i*gamma.*ax))-A)); (Bloch impedance equation)
mu=((gamma).*Zb)./(Zline.*k0);
eps=((gamma).*Zline)./(Zb.*k0);
n=((mu).*(eps));
figure;
plot(freq,imag(mu))
hold on;
plot(freq,-real(mu),'g')
xlabel('Frequency (GHz)')

```
ylabel('mueff')
legend('imaginary','real')
figure;
plot(freq,-real(eps),'g')
hold on;
plot(freq, imag(eps))
xlabel('Frequency (GHz)')
ylabel('epsiloneff')
legend('real','imaginary')
figure;
plot(freq,real(gamma*(180/pi)),'g')
hold on;
plot(freq,imag(gamma*(180/pi)))
xlabel('Frequency (GHz)')
ylabel('Phase (degree)')
legend('real','imaginary')
figure;
plot(freq, -n,'g')
xlabel('Frequency (GHz)')
ylabel('Refractive Index (n)')
legend('real')
```